ATMOSPHERIC SCIENCE

Extreme enrichment in atmospheric ¹⁵N¹⁵N

Laurence Y. Yeung, 1* Shuning Li, 1,2† Issaku E. Kohl, 2 Joshua A. Haslun, 3 Nathaniel E. Ostrom, 3 Huanting Hu, 1 Tobias P. Fischer, 4 Edwin A. Schauble, 2 Edward D. Young 2*

Molecular nitrogen (N_2) comprises three-quarters of Earth's atmosphere and significant portions of other planetary atmospheres. We report a 19 per mil (∞) excess of $^{15}N^{15}N$ in air relative to a random distribution of nitrogen isotopes, an enrichment that is 10 times larger than what isotopic equilibration in the atmosphere allows. Biological experiments show that the main sources and sinks of N_2 yield much smaller proportions of $^{15}N^{15}N$ in N_2 . Electrical discharge experiments, however, establish $^{15}N^{15}N$ excesses of up to +23‰. We argue that $^{15}N^{15}N$ accumulates in the atmosphere because of gas-phase chemistry in the thermosphere (>100 km altitude) on time scales comparable to those of biological cycling. The atmospheric $^{15}N^{15}N$ excess therefore reflects a planetary-scale balance of biogeochemical and atmospheric nitrogen chemistry, one that may also exist on other planets.

Copyright © 2017
The Authors, some rights reserved; exclusive licensee
American Association for the Advancement of Science. No claim to original U.S. Government Works. Distributed under a Creative
Commons Attribution
NonCommercial
License 4.0 (CC BY-NC).

INTRODUCTION

Nitrogen is a major component of many planetary atmospheres. On Earth, it probably first appeared early, degassing from the mantle because of its low solubility in oxidized silicate melts (1, 2). Its present-day budget is dominated by biological cycling. Nitrogen fixation (natural + industrial) is the major sink of N₂, whereas denitrification (via nitrate or nitrite reduction and ammonia oxidation) is its major source. Global rates are typically estimated to be between 400 and 500 TgN year $^{-1}$ (3–5), with a total atmospheric inventory of 3.92 \times 10 9 TgN. Abiotic N₂ cycling mechanisms are much slower and include N₂ fixation by lightning (~5 TgN year $^{-1}$) and geologic outgassing [0.1 TgN year $^{-1}$ (6)]. This vast difference in magnitude between biotic and abiotic fluxes suggests that N₂—particularly its isotopic composition—records biological nitrogen cycling at the planetary scale. A planetary-scale perspective on nitrogen cycling would offer new opportunities to evaluate Earth's enigmatic nitrogen budget.

We describe a new isotopic tracer that unlocks this signal by exploiting natural variations in $^{15}N^{15}N$, the N_2 molecule containing two rare isotopes. The tracer characterizes the relative natural abundances of $^{14}N^{14}N$, $^{14}N^{15}N$, and $^{15}N^{15}N$ as a Δ_{30} value, which quantifies the excess in $^{15}N^{15}N$ relative to a random distribution of ^{15}N and ^{14}N atoms in N_2 molecules. Mathematically, the Δ_{30} tracer is defined by $\Delta_{30}\equiv ^{30}R/(^{15}R)^2-1$, where $^{30}R=^{15}N^{15}N/^{14}N^{14}N$ and $^{15}R=^{15}N/^{14}N$. Other isotopic notations used throughout include $\delta^{15}N$, $\delta^{29}N_2$, and $\delta^{30}N_2$, defined similarly: $\delta^{15}N=^{15}R/^{15}R_{air}-1$, $\delta^{29}N_2=^{29}R/^{29}R_{air}-1$, and $\delta^{30}N_2=^{30}R/^{30}R_{air}-1$, where $^{29}R=^{14}N^{15}N/^{14}N^{14}N$. All δ and Δ_{30} values are reported in per mil (‰).

At isotopic equilibrium, a small $^{15}N^{15}N$ excess is expected because of its higher thermodynamic stability compared to $^{14}N^{14}N$ and $^{14}N^{15}N$ molecules. Thermodynamic control of Δ_{30} values would cause them to vary monotonically between 1.9 and 0.07% for temperatures between 200 and 1000 K, respectively (fig. S1) (7). When out of isotopic equilibrium, however, they may express a wider range of values that reflect biogeochemical processing (8–11). Crucially, the Δ_{30} value is mainly sensitive to the chemistry that makes and breaks N–N bonds, allowing

it to evolve independently from the 15 N/ 14 N ratio in N $_2$ on time scales governed by the rates at which its bonds are broken and remade: The Δ_{30} value traces N–N bond-forming chemistry by quantifying the number of naturally occurring 15 N-atom pairs. We analyzed the Δ_{30} composition of N $_2$ from a variety of natural and laboratory samples to an estimated accuracy of $\pm 0.3\%$, free of isobaric interferences, using an ultrahigh-resolution isotope ratio mass spectrometer (12). The measurements were calibrated against N $_2$ gas that was driven to isotopic equilibrium by reordering on a strontium nitride catalyst at 800°C.

RESULTS

Air sampled from the University of California, Los Angeles (UCLA) and Rice University shows a 19‰ excess in $^{15}{\rm N}^{15}{\rm N}$ relative to ${\rm N}_2$ containing a random distribution of $^{14}{\rm N}$ and $^{15}{\rm N}$ isotopes [that is, $\Delta_{30}=19.1\pm0.1\%$ (95% confidence interval); Fig. 1]. Stratospheric air sampled at 32 km in 2004 (*13*, *14*) and dissolved air sampled from the surface ocean in 2017 are analytically indistinguishable from surface air (table S1; P>0.4). The atmosphere's high Δ_{30} value is 10 times larger than that for thermodynamic equilibrium in its coldest regions (that is, $\Delta_{30}\sim2\%$ at 180 K), indicating that the atmospheric Δ_{30} value is governed by kinetic processes. The stratospheric sample suggests that the Δ_{30} value is homogeneous up to at least 32 km.

To determine the effects of biological cycling on the Δ_{30} value of N₂, we analyzed (i) N₂ produced by cultures of denitrifying bacteria and (ii) ¹⁵N¹⁵N isotopic fractionation factors for nitrogen-fixing cyanobacteria. Axenic cultures of Pseudomonas stutzeri and Paracoccus denitrificans produced N_2 with Δ_{30} values ranging from 0.4 to 1.4‰, with a decreasing trend as the reaction progressed. The denitrification Δ_{30} values for high nitrate conversion are lower than those for isotopic equilibrium at the culturing temperatures ($\Delta_{30,equil} = 1.0\%$ at 303 K), indicating that kinetic and/or combinatorial isotope effects are expressed in biological denitrification (table S2). Isotopic fractionation resulted in either no change or a slight decrease in Δ_{30} values for nitrogen fixation in batch cultures of Anabaena variabilis expressing the molybdenum-containing variant of nitrogenase (Fig. 1 and table S1). This observation implies that the ¹⁵N¹⁵N/¹⁴N¹⁴N isotopic fractionation factor for N2 fixation is roughly equal to the square of that for 15 N/ 14 N [that is, $^{\bar{3}0}\alpha \approx (^{15}\alpha)^2$], resulting in little change to Δ_{30} values in the residual N2 reservoir during N2 fixation.

Neither bacterial denitrification nor N_2 fixation can explain the atmospheric Δ_{30} value. Moreover, the low Δ_{30} values in N_2 coming from bacterial denitrification must be offset by another process characterized by

¹Department of Earth, Environmental and Planetary Sciences, Rice University, Houston, TX 77005, USA. ²Department of Earth, Planetary, and Space Sciences, University of California, Los Angeles, Los Angeles, CA 90089, USA. ³Department of Integrative Biology and Department of Energy Great Lakes Bioenergy Research Center, Michigan State University, East Lansing, MI 48824, USA. ⁴Department of Earth and Planetary Sciences, University of New Mexico, Albuquerque, NM 87131, USA.

^{*}Corresponding author. Email: lyeung@rice.edu (L.Y.Y.); eyoung@ess.ucla.edu (E.D.Y.) †Present address: Department of Earth and Space Sciences, Peking University, Beijing 100871, China.

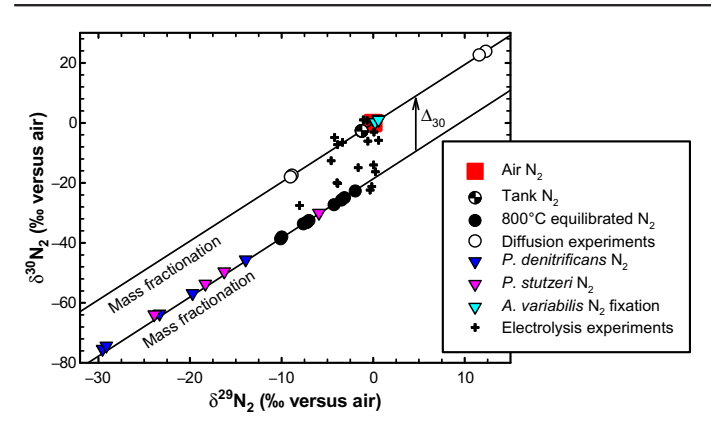


Fig. 1. Isotopic composition of N_2 from natural samples and laboratory experiments. The covariation of all three isotopic variants of N_2 is shown by plotting $\delta^{30}N_2$ versus $\delta^{29}N_2$. Mass-dependent fractionation curves for air and high-temperature equilibrated N_2 are also shown. Error bars are smaller than the data points.

extremely high Δ_{30} values (>>19%). Therefore, we evaluated whether other processes relevant to the atmospheric N₂ budget can elevate atmospheric Δ_{30} values to such a degree. Fungal denitrification produces N-N bonds as N₂O and expresses different isotope effects from those found in bacteria (15, 16), but it contributes on the order of 1% to the global N₂ budget (4). Its contribution to Δ_{30} values is likely negligible on the basis of mass balance. Anaerobic ammonia oxidation (anammox) may have an important impact on atmospheric Δ_{30} values; thus, we measured N₂ samples of opportunity from an anammox reactor at the University of Utah, which had been flushed with air-N2 to render it anaerobic (17). These samples showed Δ_{30} values lower than atmospheric values (table S2), indicating that the Δ_{30} value of anammox-N₂ is less than that of the atmosphere. A large difference in ¹⁵N/¹⁴N ratios and kinetic isotope effects for ammonium and nitrite in nature (18) suggests that end-member Δ_{30} signatures for the anammox process are near or less than zero because of combinatorial effects and mass-dependent fractionation (9). Experiments with enriched cultures are needed to determine the range of Δ_{30} values characteristic of anammox-N₂ and its contributions to the global budget, but the evidence presented here suggests that it cannot explain the high atmospheric Δ_{30} value.

Mixing of N_2 reservoirs that have similar Δ_{30} values but different $^{15}N/^{14}N$ ratios can yield elevated Δ_{30} values. However, the difference in the reservoir $^{15}N/^{14}N$ ratios must be at least 300% different, larger than any thus far observed on Earth, to cause $\Delta_{30}=19\%$ upon mixing (see Materials and Methods). Other physical effects such as gravitational and thermal fractionation are mass-dependent, yielding changes in Δ_{30} value that are much smaller in magnitude than that required to explain the atmospheric Δ_{30} value (19–21).

The slow biological recycling time of N_2 in the atmosphere [~10 million years (My) based on the N_2 inventory and biological fluxes] suggests that atmospheric chemistry could affect its isotopic composition. Extreme $\delta^{15}N$ enrichments (>500% versus Earth's N_2) have been observed in the atmospheres of Mars (22, 23) and Titan (24), possibly arising from unusual isotope effects in photochemistry near the N_2 dissociation threshold (80 to 100 nm; 12.4 to 15.5 eV) (25–27). These and other unconventional isotopic fractionation mechanisms may also be operating in the middle and upper atmosphere of Earth, influencing both the $^{15}N/^{14}N$ ratios and the proportions of $^{15}N^{15}N$ in atmospheric N_2 .

We tested this possibility by conducting high-voltage radio-frequency discharge experiments with an Oudin coil to simulate the chemistry of

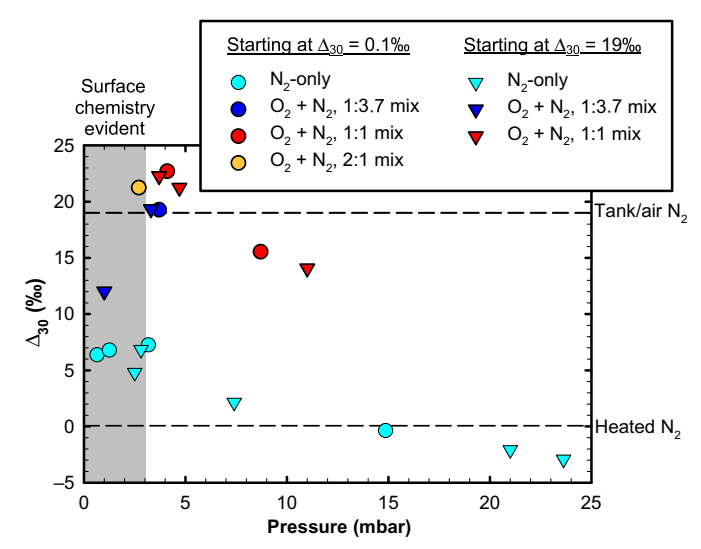


Fig. 2. Results of laboratory electrolysis experiments demonstrating clumped-isotope reordering. Initial isotopologue compositions were either N_2 that had been equilibrated at 800°C (circles) or pure tank N_2 (triangles). Surface chemistry effects likely became dominant below ~3 mbar. Error bars are smaller than the size of the data points.

 N_2 in the upper atmosphere. Pure N_2 gas and O_2/N_2 mixtures were introduced into a glass vacuum chamber that contained electrical feedthroughs made of tungsten. Experiments lasting 1 hour yielded N_2 with Δ_{30} values ranging from -3 to +23%, with a marked dependence on initial pressure and O_2/N_2 ratio (Fig. 2 and table S3). The Δ_{30} values of electrolyzed N_2 show a step-like increase when O_2 is added, and they decrease with increasing pressure above $\sim\!\!3$ mbar. Partial isotope equilibration on tungsten surfaces may be important below this pressure (28). The pressure dependence of postelectrolysis Δ_{30} values above 3 mbar is independent of the initial isotopic composition, suggesting that a laboratory steady state is approached under these conditions and that N_2 bonds are being broken and remade. Together, these experiments demonstrate that gas-phase chemistry of N_2 and its ions can potentially explain the extreme Δ_{30} values observed in the atmosphere.

The marked increase in Δ_{30} values with the addition of O_2 in the experiments points to an oxygen-containing species in the key $^{15}\text{N}^{15}\text{N}$ -concentrating step(s). The decrease in steady-state Δ_{30} values with increasing pressure suggests that this step becomes less important at higher pressures. At these higher pressures, the system is affected more by a step that disfavors ¹⁵N-¹⁵N bonds. This balance between two opposing reactions would qualitatively explain the laboratory steady state. Our kinetic model of the experiments (29) suggests that the most important N-N bond-breaking mechanisms are electron impact dissociation (N $_2$ + $e^- \rightarrow$ N $^+$ + N + $2e^-$) and the ion-molecule reaction $N_2^+ + O \rightarrow NO^+ + N$. Nitrogen-nitrogen bond-making occurs fastest via N + NO \rightarrow N₂ + O. These reactions compete primarily with recombination on chamber surfaces and gas-phase recombination (that is, $N + N + M \rightarrow N_2 + M$, where M is a third body or wall). On the basis of the dramatic increase in Δ_{30} values when O_2 is introduced, we hypothesize that the N_2^+ + O and/or N + NO reactions are key to concentrating ¹⁵N in ¹⁵N¹⁵N molecules in the laboratory experiments: Both reactions require an oxygen source and they contribute a larger proportion to the total N-N bond recycling rate as pressure decreases. The other reactions involving oxic species comprise minor channels, typically several orders of magnitude slower (fig. S4). We note that any trace oxygen source in the N_2 -only experiments (for example, from a surface; it need not be O_2) could be responsible for the pressure dependence for Δ_{30} values observed there. However, a Δ_{30} pressure dependence for the N_2 -only chemistry cannot be ruled out.

In the atmosphere, N₂⁺, NO, N, and O are also key species, particularly in the thermosphere (100 to 500 km altitude). We estimated the time scale of photochemical N₂ cycling in the atmosphere using species concentrations derived from the Whole Atmosphere Community Climate Model, eXtended version (WACCM-X) model, from the surface to ~500 km (30), and temperature-dependent reaction rates. We find that in model year 2001, 302 TgN is recombined via N + NO, whereas 0.01 TgN is recombined by the $N + NO_2$ and $N^+ + NO$ channels combined (Fig. 3). The most important chemical channel of N₂ destruction, N₂⁺ + O, destroys about 74 TgN year⁻¹. Photolytic, electrolytic, and nonthermal N2 bond rupture cannot be explicitly calculated from the WACCM-X species concentrations; hence, we assume that the sum of all destruction mechanisms balances chemical recombination to maintain a steady state for N₂ concentrations. In such a steady state, the thermosphere would recycle a mass of N₂ equal to the atmospheric inventory $(3.92 \times 10^9 \, \text{TgN})$ in 13 My. Locally nonthermal conditions in the thermosphere and variations in incident solar radiation can alter this estimate (see Supplementary Text). Nevertheless, the time scale of atmospheric N2 recycling is likely comparable to that for biological N₂ cycling.

Furthermore, mass exchange between the upper and lower atmosphere is sufficient to mix high- Δ_{30} thermospheric N_2 into the troposphere on these time scales. The anthropogenic CO_2 rise has recently been detected in the lower thermosphere by satellites (31, 32), suggesting that gases emitted at the surface can enter the thermosphere within several hundred years and vice versa. The atmosphere's Δ_{30} value therefore carries signatures of both gas-phase and biological processing of N_2 .

DISCUSSION

We interpret the atmospheric Δ_{30} value in N_2 (hereafter $\Delta_{30,atm}$) as the balance between two planetary-scale cycles that drive Δ_{30} toward characteristic end-member values. Atmospheric chemistry, primarily in the thermosphere, drives $\Delta_{30,atm}$ toward its end-member value, $\Delta_{30,\text{thermosphere}}$, at a rate represented by $F_{\text{thermosphere}}$ (TgN year⁻¹). Biological N_2 cycling drives $\Delta_{30,atm}$ toward its end-member value $\Delta_{30, \mathrm{bio}}$ at the rate F_{bio} . Our data suggest that N_2 fixation does not alter atmospheric Δ_{30} values significantly (that is, it does not discriminate strongly and fractionates mass-dependently); thus, the biological signature of $\Delta_{30 \text{ bio}}$ is primarily that associated with denitrification. The steady-state global Δ_{30} mass balance is thus approximately described by $F_{\text{bio}}(\Delta_{30,\text{atm}} - \Delta_{30,\text{bio}}) + F_{\text{thermosphere}}(\Delta_{30,\text{atm}} - \Delta_{30,\text{thermosphere}}) \approx 0$ (see Supplementary Text). Using $\Delta_{30,\text{bio}} = 0.4\%$ and the WACCM-X-derived $F_{\text{thermosphere}} = 302 \text{ TgN year}^{-1}$, we find that $\Delta_{30,\text{thermosphere}} =$ 40 to 50% would be consistent with current bottom-up estimates of the global denitrification flux of N_2 ($F_{bio} \sim 400$ to 500 TgN year⁻¹; Fig. 4A). A larger Δ_{30,thermosphere} end-member value would imply a larger global biological N_2 cycling rate and vice versa. Refining $\Delta_{30,\text{bio}}$ $\Delta_{30,\text{thermosphere}}$ and $F_{\text{thermosphere}}$ may thus allow one to constrain the average global rate of denitrification integrated over the past ~10 My. In principle, this idea can also be applied to extraterrestrial atmospheres to determine rates of biogeochemical nitrogen cycling once the controls on $\Delta_{30,\text{thermosphere}}$ and $F_{\text{thermosphere}}$ (for example, those tied to solar flux and the presence of oxic species) are understood. On smaller scales, the Δ_{30} tracer should be an in situ measure of denitrification that does not rely on tracer injections and their associated uncertainties (33). It may be particularly useful for studying nitrogen cycling in oceanic oxygen minimum zones and subsurface terrestrial environments.

More broadly, Δ_{30} measurements are of utility as an unambiguous measure of air content in geochemical mixtures. For example, gases

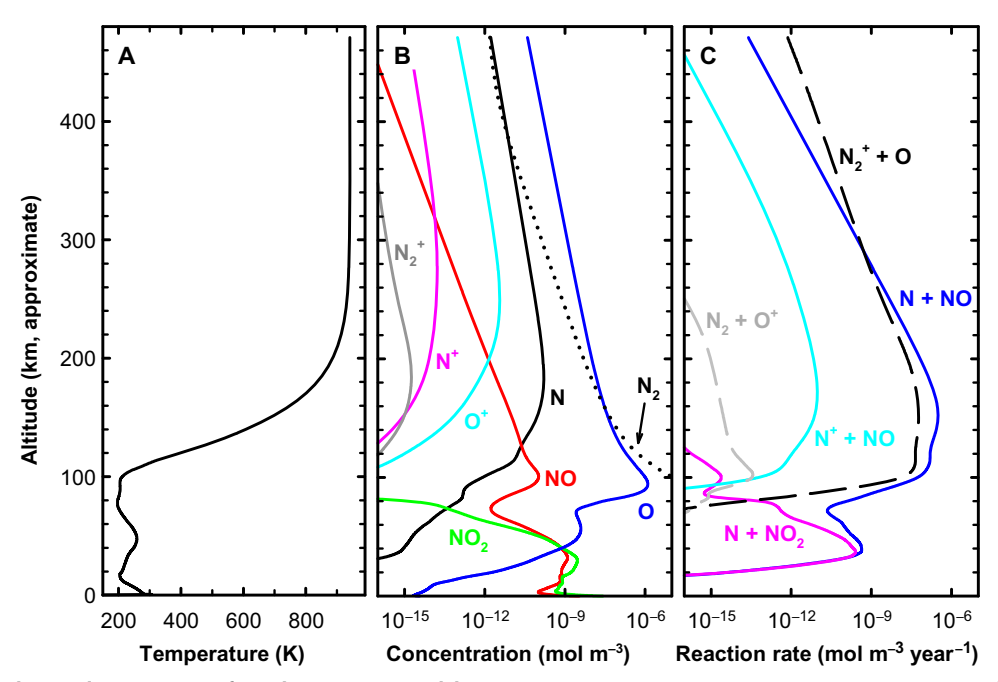


Fig. 3. Calculated global, annual mean outputs from the WACCM-X model (year 2001). (A) Temperatures, (B) species concentrations, and (C) gas-phase thermal reaction rates relevant to N-N bond rupture and formation are shown. Nonthermal effects are important in the upper atmosphere but are not included in these calculations. Photolysis reactions have been omitted from this plot.

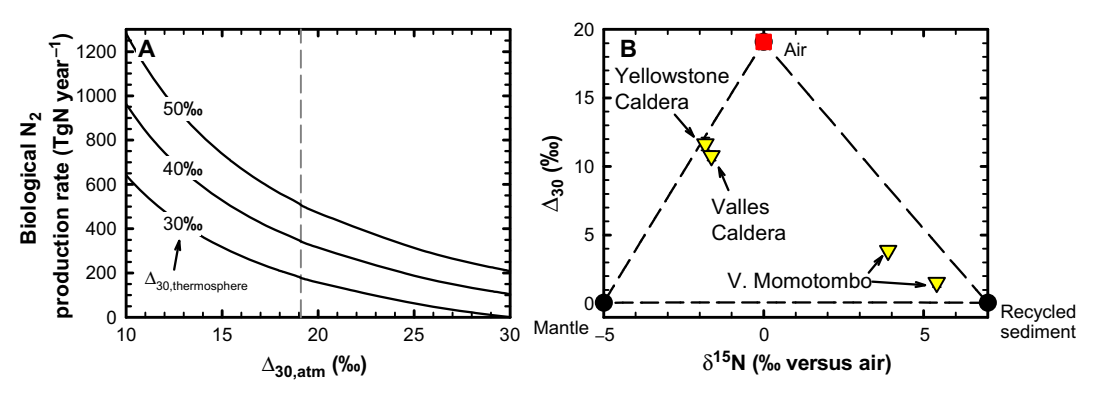


Fig. 4. Applications of the Δ_{30} tracer. Using atmospheric Δ_{30} values to constrain the global denitrification rate (A) [the dashed line in (A) represents the current atmospheric Δ_{30} value] and the nitrogen sources of geologic N₂ outgassing (B). Error bars are smaller than the size of the data points.

that are mixtures of atmospheric N2 and geologically outgassed N2 can be partitioned into contributions from atmospheric N₂, mantle nitrogen, and crustal nitrogen using Δ_{30} values, δ^{15} N values, and isotopic mass balance in N2 (Fig. 4B). For high-temperature geologic nitrogen sources, Δ_{30} signatures are expected to be low because of combinatorial effects or isotope exchange equilibrium (for example, $\Delta_{30} = 0.07\%$ at 1000 K), whereas δ^{15} N values will reflect the source material [for example, +7% versus air for sedimentary sources and -5% for mantle sources (6, 34), although mantle δ^{15} N values may be lower (35)]. The residence time of gases in hydrothermal systems (weeks or less) is short relative to time scales of isotopic equilibration in those environments (that is, T < 400°C without engineered catalysts; see heating experiments in Materials and Methods); air is expected to retain its high Δ_{30} value under such conditions. The Δ_{30} value of N₂ from fumaroles should therefore allow one to quantify the proportion of air in the sample, whereas the $\delta^{15}N$ value can be used to partition the remaining nitrogen between mantle and recycledsediment sources.

Fumarole gases collected at the summit crater of the Momotombo volcano (36), in the Nicaraguan volcanic front, show low Δ_{30} values of 1.5 and 3.9%. Gases drawn from fumaroles in Valles Caldera (New Mexico, USA) and Yellowstone Caldera (Wyoming, USA) show higher Δ_{30} values (10.8 and 11.6‰, respectively), indicating a higher proportion of background air contribution. We find that 82 and 91% of the volcanic nitrogen in the Momotombo samples come from subducted sediment sources. The caldera samples, representing mantle hot spots or continental rifts with little influence from subducted sediments, contain primarily mantle-derived N₂: 11 and 3% of the nonatmospheric N2 come from sedimentary N2 at Valles Caldera and Yellowstone Caldera, respectively. Although noble gas-based source apportionment yields similar subducted sediment fractions for the Momotombo samples (86 and 94%, respectively), they disagree for the Yellowstone Caldera sample (3% sedimentary from Δ_{30} values versus 19% from N₂/He ratios; table S5). Signatures of mantle and crustal outgassing are variable, and postsampling gas loss will affect gas species ratios much more so than isotopic ratios; hence, the combined Δ_{30} - δ^{15} N approach is likely more robust for these questions. Applying the Δ_{30} tracer to volcanic N₂ outgassing may constrain the ¹⁵N isotopic composition of the primordial mantle, which has implications for planetary accretion, differentiation, and the development of the early atmosphere (37).

MATERIALS AND METHODS

Analytical methods

Natural and laboratory-generated samples of N_2 were analyzed on an ultrahigh-resolution gas source mass spectrometer that separates $^{14}N^{14}N$, $^{14}N^{15}N$, and $^{15}N^{15}N$ from their main isobaric interferences (12). Spike-dilution experiments suggest that residual isobaric effects on N_2 are minor, comparable to other analytical uncertainties. Measurements were calibrated to a thermodynamically based reference frame by equilibrating N_2 gases at 800°C with strontium nitride (fig. S1) (38). Methodological accuracy was verified using the pinhole-diffusion and N_2 re-equilibration experiments described below.

 N_2 gas was analyzed at mass/charge ratio (m/z) = 28, 29, and 30 (14N14N+, 14N15N+, and 15N15N+, respectively) on the Nu Instruments Panorama mass spectrometer (UCLA). ¹⁴N¹⁴N⁺ and ¹⁴N¹⁵N⁺ ions were collected on Faraday cups with intensities ranging from 15 to 480 pA for ¹⁴N¹⁴N⁺, with all natural samples but the volcanic samples run between 50 and 480 pA. Volcanic samples were run between 18 and 50 pA. A secondary electron multiplier was used for $^{15}\text{N}^{15}\text{N}^+$, with corresponding count rates ranging from 1×10^3 to 4×10^4 counts per second (cps), or 0.06 to 2.5 fA. Abundances of ¹⁴N¹⁴N, ¹⁴N¹⁵N, and ¹⁵N¹⁵N in atmospheric N₂ are approximately 99.3%, 0.7%, and 14 parts per million, respectively. Typical mass resolving power (MRP) was near 50,000, calculated as the ratio of the ion mass and the mass difference between 95 and 5% of the peak height; for example, MRP = 30.00022 atomic mass unit (amu)/0.0006 amu = 50,000. Nearly baseline resolution is achieved between ¹⁴N¹⁶O⁺ and ¹⁵N¹⁵N⁺, despite a mass difference of only 0.002 amu (fig. S2). Replicate Δ_{30} measurements of air with $^{14}N^{16}O^{+}$ ion currents ranging from 10⁴ to 10⁵ cps, afforded by having previously reduced the source surfaces with methane, were indistinguishable. The effect of the isobaric interference between ¹²C¹⁸O⁺ and ¹⁵N¹⁵N⁺ (mass difference, 0.001 amu) was evaluated using serial ¹²C¹⁸O spike dilutions and found to be comparable to the uncertainty in the external reproducibility of the measurement (fig. S2).

Samples of N_2 were purified using gas chromatography (GC) with methods described previously for methane (11). Briefly, a two-column setup at 60°C was used to separate N_2 from other gases, first through a stainless steel molecular sieve 5A column [3 m × 1/8" outside diameter (OD)] followed by a stainless steel HaySep D column (2 m × 1/8" OD). This setup was interfaced with an all–stainless steel, oil-free high-vacuum line (base pressure ~10⁻⁶ mbar) through which samples were introduced

and recollected for analysis. Some air samples were purified on a separate, single-column GC system (30 to 60 cm \times 1/8" OD molecular sieve 5A, 80/100 mesh) over a range of temperatures, interfaced with a glass vacuum line (19), with indistinguishable results.

Calculations, instrument calibration, and testing

The bulk ¹⁵N/¹⁴N ratio, in terms of ¹⁴N¹⁴N, ¹⁴N¹⁵N, and ¹⁵N¹⁵N abundances, is expressed as

$${}^{15}R = {15 \choose {14 \choose 1}} = \frac{{}^{14}N^{15}N + 2^{15}N^{15}N}{2^{14}N^{14}N + {}^{14}N^{15}N} = \frac{{}^{29}R + 2^{30}R}{2 + {}^{29}R}$$
(1)

Therefore, to obtain both a $\delta^{15} N \equiv (^{15}R_{\text{sample}}/^{15}R_{\text{air}}-1)$ value and a Δ_{30} value, one must solve for ^{15}R of the sample using ^{29}R and ^{30}R . Our method is one often used in clumped-isotope geochemistry, namely, to measure a $\delta^{15}N$ standard (air; $^{15}R_{\text{air}}=0.003676$) and a Δ_{30} standard (N_2 isotopically equilibrated at 800°C; see fig. S1) against the same laboratory working standard gas and iterate ^{29}R and ^{30}R of that gas until its isotopic composition is found. Subsequent measurements are related to the $\delta^{15}N$ and Δ_{30} standards through this working gas.

We note in passing that Eq. 1 also shows how mixing between N_2 reservoirs will alter ^{15}R nonlinearly. Moreover, because $\Delta_{30} \equiv ^{30}R/(^{15}R)^2-1$, Δ_{30} values vary nonlinearly with mixing as well. A 50:50 mixture between components that both have Δ_{30} values of zero, but with a 20% difference in $\delta^{15}N$, will have $\Delta_{30} = +0.1\%$. If the difference in $\delta^{15}N$ of the two components is 40%, then the gas will be characterized by $\Delta_{30} = +0.4\%$.

In order to reorder N₂ toward high-temperature equilibrium, samples were expanded into either breakseals or valved quartz sample tubes containing strontium nitride (Sr₃N₂, a black powder; ESPI Metals and Materion) and heated in a horizontal tube furnace to 800°C for between 4 and 96 hours. Time-series experiments conducted at 400° and 800°C (Δ_{30} = 0.21 and 0.07‰ at equilibrium, respectively) showed a ninefold change in reordering rate (fig. S2), but we also found that this rate depended on the age of the solid catalyst; it decomposes slowly over time due to reaction with water to make ammonia. The condition of the catalyst and the relative proportions of catalyst to N2 gas allowed some variation of δ^{15} N values of the equilibrated gas (table S1). We also reordered N_2 from a 21-mbar electrolysis experiment (Δ_{30} = -2%) to $\Delta_{30} = 0.0 \pm 0.1\%$ on strontium nitride at 800°C. This experiment, combined with the time series described above, indicates that heating N₂ over strontium nitride yields N₂ with a nearly random distribution of isotopes.

In general, the catalyst is crucial to the isotopic reordering of $N_2.$ An experiment using titanium nitride instead of strontium nitride as the N_2 -reordering catalyst showed significantly slower reordering ($\Delta_{30}=19\rightarrow7\%$ in 7 days at 900° to 1000°C) with no change in $\delta^{15}N.$ The experiment suggests that the N_2 isotopes are not equilibrating on the quartz.

To verify instrumental accuracy with pure N_2 samples, we performed pinhole-diffusion experiments using the same apparatus as that described previously for O_2 (19). Briefly, 1 mbar of N_2 in a 5-liter bulb was allowed to diffuse through a 75 \pm 7.5 μm critical orifice, which was comparable to the mean free path of N_2 at that pressure (~95 μm). The amount of undiffused gas remaining was determined manometrically, and both the diffused gas and the residue gas were analyzed to determine the difference in their $\delta^{29}N_2$ and $\delta^{30}N_2$ values.

Measured values were in agreement with those predicted for Rayleigh fractionation of gases separated according to Graham's law of effusion within typical analytical uncertainty ranges (that is, $\pm 0.2\%$ in $\delta^{30} N_2$) when a correction for back diffusion/viscous flow was included (table S6). The correction in which the effective fractionation factor $\alpha_{\rm effective}$ is related to Graham's law fractionation factor $\alpha_{\rm effusion}$ by $(\alpha_{\rm effective}-1)=(\alpha_{\rm effusion}-1)(1-P_{\rm ds}/P_{\rm us})$ has been described previously; the $P_{\rm ds}/P_{\rm us}$ factor here is similar in magnitude to that found previously on the same apparatus for O_2 diffusion (19). The consistency between theory and measurements for these experiments suggests that isotopic reordering on the tungsten filament in the mass spectrometer does not exceed analytical uncertainties over a range of ${\sim}40\%$ in $\delta^{30}N_2$.

Other potential impurities in natural samples included O_2 and methane. We performed analyses of air- N_2 that included up to 14% O_2 and found that Δ_{30} values increase 0.5‰ at 3 to 4% O_2 and 1.8‰ at 14% O_2 , accompanied by 0.2 and 0.5‰ decreases in $\delta^{15}N$ values, respectively. We estimate typical O_2 content to be <<1% after GC purification. In the volcanic N_2 samples, small amounts of methane (<10%) were identifiable and collected in the tail of the N_2 peak. To examine the effect that this methane impurity may have on the N_2 isotopologue ratios, we made a 10% methane/ N_2 mixture of similar sample size and purified it. We did not observe any difference in Δ_{30} value from the methane-free tank gas.

Finally, we tested for potential analytical artifacts due to variations in N_2 sample size. Air- N_2 samples ranging from 5 to 160 μ mol in size were prepared and analyzed over a range of ion currents. Bulk isotope composition exhibited larger variability at small sample sizes, about $\pm 0.2\%$ in δ^{15} N versus $\pm 0.05\%$ for larger samples. The Δ_{30} values were indistinguishable up to ~250 pA on m/z = 28 (smaller samples had larger analytical uncertainty because of counting statistics). Above 250-pA ion currents, the Δ_{30} values for air-N₂ decreased by as much as ~0.4% when the ion current was 400 pA on m/z = 28. The origin of this effect is enigmatic: No dependence on ion current intensity was observed for heated gases, and ion-counting rates (10⁴ cps) were lower than typical rates that one expects would require dead-time corrections. A possible explanation for this effect is isotope exchange between NO and N_2 in the ion source, similar to the exchange reaction observed for N₂O (39). Whatever the source of this ion-intensity effect, it was only relevant for N₂ dissolved in seawater (the largest samples), and the effects are small. We therefore report Δ_{30} values for those samples before and after correcting for this ion-intensity effect based on the air-N₂ measured at similar ion currents (table S1). On the basis of the comprehensive analytical tests above, we estimate an overall accuracy of $\pm 0.3\%$ in Δ_{30} values.

Natural samples

Sampling procedures for UCLA air and the stratospheric sample have been described previously (14, 19). The stratospheric sample was #3-A01-R(1141) from a scientific balloon flight in 2004 (Fort Sumner, New Mexico; 32.3 km) that has also been characterized for a variety of other trace gases and isotope ratios (14, 19, 40, 41). The stratospheric air samples were purified at UCLA. Seawater samples were collected from the San Pedro Ocean Time-series site ($33^{\circ}33'$ N, $118^{\circ}24'$ W), a coastal site near Los Angeles, on 12 April 2017. They were siphoned from 10-liter Niskin flasks into prepoisoned, pre-evacuated ($<10^{-3}$ mbar) bottles according to established methods (42). The bottles were allowed to degas and equilibrate on an orbital shaker (110 rpm) for 48 hours before the water was removed, and the headspace gas was collected onto silica gel for purification. Dissolved N_2 was separated

from the other gases at Rice University on a molecular sieve 5A column (3.05 m \times 1/8" OD, 80/100 mesh) at -80°C and recollected on a silica gel U-trap using a method described previously (41). We also isolated atmospheric N_2 using this method, and the results were indistinguishable from gases collected and purified at UCLA.

Biological culturing conditions and experiments Denitrifying bacteria

P. stutzeri and *P. denitrificans* were cryogenically stored (-80°C) in tryptic soy broth (TSB; Caisson Labs) and sterile glycerol 1:1 (v/v). Stock cultures were reestablished in 5 ml of TSB amended with sodium nitrate (NaNO₃, 10 mM; Sigma-Aldrich) under aerobic conditions at a constant temperature with continuous agitation (18 hours). Denitrifier cultures were grown at 30°C. Individual colonies were obtained from reestablished stock cultures by the streak-plate technique on tryptic soy agar (Caisson Labs) amended with NaNO₃ (10 mM). Streak-plate cultures were sealed with parafilm and incubated (aerobic, 30°C). The plates were stored at 4°C for up to 2 weeks before establishment in liquid medium for experiments.

The two species were established with one colony from stored stock culture plates in 5 ml of TSB amended with NaNO₃ (10 mM) in a 20-ml culture tube (Thermo Fisher Scientific). Cultures were grown aerobically with agitation (30°C for 18 hours) to late exponential phase (optical density at 600 nm = 2.0). Culture turbidity was determined with a Spectronic 20 spectrophotometer (Bausch and Lomb). Two 160-ml sterile serum bottles containing 50 ml of carbon minimal medium (CMM; 10 mM NaNO₃ and 10 mM sodium succinate; Sigma-Aldrich) (43) were each inoculated with 200 µl of the aerobic culture. The bottles were stoppered (Geomicrobial Technologies Inc.) and crimp-sealed, and the headspace was sparged with ultrahigh purity (UHP) helium for 20 min. Cultures were incubated (30°C for 18 hours) with agitation. The cells were transferred to 50-ml conical Falcon tubes (Corning) and centrifuged (3000g for 30 min). The cell pellet was washed in CMM lacking carbon and nitrogen and centrifuged (3000g for 30 min). The supernatant was decanted, and the cells were dispersed in CMM lacking a carbon or nitrogen source (optical density at 600 nm = 0.2). The cells were aliquoted (9.6 ml) into sterile flasks outfitted with a vacuum "sidearm" valve (160 ml), and a carbon source was added (30 mM sodium succinate). The flask was stoppered (Geomicrobial Technologies Inc.) and crimp-sealed, and the sidearm closure was sealed. An anaerobic environment was created by sparging the cells (UHP He, 60 min). Sparging was accomplished by inserting one sterile stainless steel needle (#20, Thomas Scientific) carrying He gas through the stopper into the medium while a second sterile stainless steel needle was inserted through the stopper and into the headspace to allow gas to exit. Following sparging, the flasks were allowed to reach atmospheric pressure and then the reactions were initiated by injecting the nitrogen source (30 mM USGS34 potassium nitrate) with a gas-tight syringe. Individual reactions were stopped by injecting 10 M sodium hydroxide (400 µl).

Nitrogen-fixing cyanobacteria

A. variabilis [American Type Culture Collection (ATCC) 29413] was cultivated in BG-11 medium (44) from lyophilized samples as per ATCC instructions. Cultures were maintained by streaking onto BG-11 agar under a 12-hour light/12-hour dark regime at 25°C.

Cyanobacterial cultures were started from streak plates of *A. variabilis* by adding culture to 10 ml of BG-11 medium and incubating aerobically (22°C, 12-hour light/12-hour dark regime). Cultures were transferred to larger vessels twice in 1:10 dilutions to reach a final culture volume of 250 ml. Transfers were conducted only when cultures reached a

chlorophyll-a density of greater than 1 µg/ml (45). The cells were centrifuged (4000g for 15 min) and washed 1× in 50 ml of BG-11 medium without nitrogen (BG-11_o). The cells were resuspended in 250 ml of BG-11_o medium, which had been allowed to equilibrate with laboratory air for 1 day with gentle stirring. Contamination of outside agents was prevented by fitting a sterile cotton plug to the flask opening and covering this with sterile tin foil. Laboratory equilibration of the medium served to ensure that atmospheric N₂ was the only source of nitrogen in the medium. The culture was then transferred to a sterile "Emerson" flask with a sterile gravity syphon. The Emerson flask (200 ml) was filled beyond the neck and then sealed shut to remove any headspace. Before stoppering the flask, the seal was sterilized with 70% ethanol and rinsed with Milli-Q water. Nitrogen fixation reactions were considered to have begun once the Emerson bottle was stoppered. Reactions were conducted in an environmental chamber (22°C, 12-hour light/12-hour dark regime), and the flasks were turned over once a day to provide gentle agitation. After between 2 and 7 days, the dissolved N₂ was transferred by equilibration following established protocols (42). After allowing the culture to settle to the bottom of the bottle, 150 ml of culture medium was transferred to an evacuated Emerson bottle (300 ml) with a sterile syphon. The transferred medium was allowed to equilibrate for at least 6 hours before isolation.

Isolation and trapping of N2 for analysis

Quantitative distillation of N_2 from samples was achieved under high vacuum (4.5 µmHg). A metering valve and two stainless steel liquid N_2 cryogenic traps (OD = 6.35 mm) preceded the sample bottle. The first cryogenic trap condensed and separated water from gases, whereas the second trap was filled with coarsely crushed silica to trap all remaining gases (15 min). Isolated N_2 was cryogenically transferred to a 30-cm Pyrex tube (OD = 6.35 mm) containing 50 mm of crushed silica gel for 15 min. To accomplish this, the second cryogenic trap was isolated from the first cryogenic trap and the vacuum line was evacuated. The system was then isolated from the vacuum system and the isolated gases were desorbed from the silica by heating with warm tap water. Pyrex sample tubes were sealed with an acetylene torch while still under cryogen conditions. All silica gel traps were conditioned under high vacuum at 200°C (24 to 48 hours) before sampling.

The specific method for isolation of N_2 from sidearm flasks for denitrification experiments differed slightly from the previous method. Sidearm bottles were attached to the vacuum line with ultra-torr Cajon fittings. The sidearm bottle was opened to the vacuum line while the metering valve remained closed. The metering valve was then slowly opened to maintain a vacuum (50 to 70 $\mu mHg)$ while the sample passed through the cryogenic traps, until high vacuum was again achieved (35 to 40 min). The cryogenically isolated gases were then desorbed from the silica as previously described.

Analytical correction for air contamination

During the *P. denitrificans* experiments, a procedural blank was performed, which revealed a small residual gas pressure equal to 1 to 5% of the experimental N_2 gas yield, depending on reaction progress. This blank (0.8 µmol) was presumed to be entirely N_2 with atmospheric isotopic composition. The reported isotopic composition for both the *P. denitrificans* and the *P. stutzeri* experiments includes a correction for this blank. We cannot rule out a difference in blank amount between the two experiments. However, the more fully reacted experiments had larger N_2 gas yields and therefore a smaller contamination from this blank; thus, their Δ_{30} values are more likely to reflect those intrinsic to bacterial denitrification.

Samples of opportunity from anammox bioreactors

Water from a semi-batch–fed anammox bioreactor at the University of Utah (17) was sampled into 60-ml septa vials (bubble-free, until they overflowed, ensuring no gas headspace) and poisoned with 600 μ l of saturated ZnCl₂ solution. Samples were shipped back to Michigan State University for isolation of the dissolved gases.

Electrolysis experiments and modeling Laboratory electrolysis

Electrolysis experiments were performed in a valved-off Bayart-Alpert ion gauge with one lead (the ion collector) attached to the Oudin coil and the others grounded (fig. S3). The chamber was preconditioned initially by applying a voltage to the electrical lead under vacuum for ≥ 1 hour to degas the filament and then applying a voltage under N_2 atmosphere for ≥ 1 hour to replace the adsorbed species with nitrogen. In the experiments, voltage was applied to the electrical lead until continuous visible emission was observed in N_2 or an O_2/N_2 mixture. The same analog setting (that is, rotating dial position at the base of the coil) was used for all samples. The reaction was allowed to proceed for 1 hour.

The emission field changed color and expanded as pressure was varied (fig. S3). The colors and patterns were similar for both N_2 only and O_2/N_2 mixtures. These changes suggest that local electron and ion concentrations and electron energies also varied with pressure. Consequently, we expect that ion production rates, energy-dependent product branching ratios, wall reaction rates, and the rates of reactions dependent on these quantities likely varied with total pressure as well. Because of the potential variability in reaction rates expected in the experiments, our kinetic model was aimed at determining the most important N-N bond-altering mechanisms in the gas phase rather than explaining the laboratory results quantitatively.

Model of electrolysis experiments

The model contained 41 reactions for the O_2 - N_2 system, including charge transfer reactions (table S4). It was run at 298 K for 1 hour of simulated time using the program Kintecus (29). Electron temperatures were held constant at 10,000 K. Only positive ion chemistry was included except for electron impact and recombination processes. Electronic states were not specified; ground electronic states and thermal vibrational states for all reactions and products were assumed unless otherwise noted. Surface chemistry was not explicitly included. Electron impact ionization was only included for N_2 and O_2 , with prescribed (but adjustable) branching ratios between ionization and fragmentation channels (typically 3:1). A more explicit description would render the number of variables unmanageable for this conceptual model. In a similar vein, electron densities were prescribed and held constant within each simulation as a way to specify the total rate of electron impact processes.

Gross rates of N–N bond-altering processes were tracked by including "dummy" products in those reactions that did not affect other variables such as temperature or pressure. Rates of electron impact ionization and dissociation were varied over a large range, but rates of at least 10^{13} to 10^{14} cm 3 s $^{-1}$ were required for the fastest N–N bond-altering processes to reorder an amount of N_2 equal to the experiment's inventory between 1 and 10 mbar (2.5 \times 10^{16} to 2.5 \times 10^{17} cm $^{-3}$). For the N_2 -only experiments, only electron impact and the termolecular N + N + M \rightarrow N $_2$ + M reaction would be relevant to the destruction and formation of N_2 unless some other trace oxygenated constituent were present (for example, NO). We note that tungsten surfaces can catalyze isotope exchange between N_2 molecules

(28); at low pressures, therefore, these reactions likely influenced Δ_{30} values resulting from electrolysis, driving them down toward isotopic equilibrium values in competition with gas-phase isotopic fractionation.

Sample results for three different electron number densities are shown in fig. S4. In all cases, electron impact fragmentation of N_2 is the only important N_2 bond-breaking mechanism by an order of magnitude except at low pressures. At low pressures, $N_2^+ + O$ becomes comparable in rate. The importance of this channel decreases at higher pressures. Of the bond-making reactions, N + NO is the most important by at least a factor of 100 in all cases.

Determining the atmospheric N_2 recycling time scale

Globally integrated rates of N₂ bond-altering processes in moles per year were calculated from monthly-averaged outputs of the WACCM-X model (30) for model year 2001 (1.9° latitude \times 2.5° longitude grid). The data were outputs of present-day control runs of the Community Earth System Model version 1.0 (data set f.e10.FWX.f19 f19.control.001) available from the Earth System Grid (www.earthsystemgrid.org). Globally integrated species concentrations and reaction rates were calculated using methods similar to those previously described (41). Briefly, reaction rates were calculated at each grid point using monthlyaveraged species mixing ratios, temperatures, and pressures. Because N₂ is not an explicit field in this version of the model, its concentrations were calculated by subtracting the number densities of O and O2 from the total number density. Reaction rates were then integrated over grid volumes covering all 81 atmospheric levels using the latitude, longitude, and mean geopotential height of each grid point as the vertical coordinate. Accuracy checks on this integration scheme included reproducing the total atmospheric N_2 inventory (1.40 × 10²⁰ mol N_2 modeled versus 1.4×10^{20} mol N₂ expected) and total atmospheric volume $(2.74 \times 10^{14} \text{ km}^3 \text{ modeled versus } 2.76 \times 10^{14} \text{ km}^3 \text{ using a 500-km})$ exobase). Weighting for residence time in different regions of the atmosphere was not included because the time scale for whole-atmospheric mixing [<<10⁶ years based on cross-homopause and intrathermosphere diffusion coefficients of >10⁻⁵ km² s⁻¹ (46)] should be much faster than the time scale found for atmospheric N₂ bond recycling (10^7 years) . The time scale for atmospheric N₂ recycling in years is defined as the total N2 inventory divided by the globally integrated rate of N-N recombination assuming a steady state between N2 destruction and recombination.

Mass balance of volcanic N₂

Mixing fractions of air N_2 , recycled-sediment N_2 , and mantle N_2 in volcanic N_2 samples (that is, f_{air} , f_{RS} , and f_{mantle} , respectively) are calculated from N_2 /He ratios and $\delta^{15}N$ values using the endmember compositions shown in table S5 and the mass balance equations (36)

$$(N_2/He)_{\text{sample}}^{-1} = f_{\text{air}}/(N_2/He)_{\text{air}} + f_{\text{RS}}/(N_2/He)_{\text{RS}} + f_{\text{mantle}}/(N_2/He)_{\text{mantle}}$$
 (2)

$$\delta^{15} \mathrm{N_{sample}} = f_{\mathrm{air}} \delta^{15} \mathrm{N_{air}} + f_{\mathrm{RS}} \delta^{15} \mathrm{N_{RS}} + f_{\mathrm{mantle}} \delta^{15} \mathrm{N_{mantle}} \tag{3}$$

$$f_{\text{air}} + f_{\text{RS}} + f_{\text{mantle}} = 1 \tag{4}$$

Alternatively, they are calculated using Eqs. 4 to 6 and δ^{15} N and Δ_{30} values for each end-member (converted to ^{29}R and ^{30}R using Eq. 1)

$$^{29}R_{\text{sample}} = f_{\text{air}}^{29}R_{\text{air}} + f_{\text{RS}}^{29}R_{\text{RS}} + f_{\text{mantle}}^{29}R_{\text{mantle}}$$
 (5)

$${}^{30}R_{\text{sample}} = f_{\text{air}}{}^{30}R_{\text{air}} + f_{\text{RS}}{}^{30}R_{\text{RS}} + f_{\text{mantle}}{}^{30}R_{\text{mantle}}$$
 (6)

In both methods, only f_{air} , f_{RS} , and f_{mantle} are unknown, and they can be computed using a set of three equations.

SUPPLEMENTARY MATERIALS

Supplementary material for this article is available at http://advances.sciencemag.org/cgi/content/full/3/11/eaao6741/DC1

Supplementary Text

fig. S1. Theoretical Δ_{30} values at isotopic equilibrium ($\Delta_{30,equil}$) as a function of temperature, from Wang et al. (7).

fig. S2. Analytical tests of $\Delta_{\rm 30}$ accuracy.

fig. S3. Changes in visible emission properties during electrolysis experiments.

fig. S4. Modeled gross rates of bond-breaking (black symbols) and bond-making (red symbols) reactions in the electrolysis experiments.

table S1. Isotopic data for air samples and heated gases.

table S2. Isotopic data for biological experiments.

table S3. Data for electrolysis experiments.

table S4. Reactions used in the model of the electrolysis experiments.

table S5. Data for volcanic N_2 samples and end members used to derive mixing fractions f_{RS} and f_{maxter} .

table S6. Results from diffusion experiment for verifying instrumental accuracy. References (47–73)

REFERENCES AND NOTES

- S. Mikhail, D. A. Sverjensky, Nitrogen speciation in upper mantle fluids and the origin of Earth's nitrogen-rich atmosphere. *Nat. Geosci.* 7, 816–819 (2014).
- G. Libourel, B. Marty, F. Humbert, Nitrogen solubility in basaltic melt. Part I. Effect of oxygen fuqacity. Geochim. Cosmochim. Acta 67, 4123–4135 (2003).
- N. Gruber, J. N. Galloway, An Earth-system perspective of the global nitrogen cycle. Nature 451, 293–296 (2008).
- J. N. Galloway, F. J. Dentener, D. G. Capone, E. W. Boyer, R. W. Howarth, S. P. Seitzinger, G. P. Asner, C. C. Cleveland, P. A. Green, E. A. Holland, D. M. Karl, A. F. Michaels, J. H. Porter, A. R. Townsend, C. J. Vöosmarty, Nitrogen cycles: Past, present, and future. *Biogeochemistry* 70, 153–226 (2004).
- D. Fowler, M. Coyle, U. Skiba, M. A. Sutton, J. Neil Cape, S. Reis, L. J. Sheppard, A. Jenkins, B. Grizzetti, J. N. Galloway, P. Vitousek, A. Leach, A. F. Bouwman, K. Butterbach-Bahl, F. Dentener, D. Stevenson, M. Amann, M. Voss, The global nitrogen cycle in the twenty-first century. *Philos. Trans. R. Soc. B* 368, 20130165 (2013).
- Y. Sano, N. Takahata, Y. Nishio, T. P. Fischer, S. N. Williams, Volcanic flux of nitrogen from the Earth. Chem. Geol. 171, 263–271 (2001).
- Z. Wang, E. A. Schauble, J. M. Eiler, Equilibrium thermodynamics of multiply substituted isotopologues of molecular gases. *Geochim. Cosmochim. Acta* 68, 4779–4797 (2004).
- D. T. Wang, D. S. Gruen, B. S. Lollar, K.-U. Hinrichs, L. C. Stewart, J. F. Holden, A. N. Hristov, J. W. Pohlman, P. L. Morrill, M. Könneke, K. B. Delwiche, E. P. Reeves, C. N. Sutcliffe, D. J. Ritter, J. S. Seewald, J. C. McIntosh, H. F. Hemond, M. D. Kubo, D. Cardace, T. M. Hoehler, S. Ono, Nonequilibrium clumped isotope signals in microbial methane. *Science* 348, 428–431 (2015).
- L. Y. Yeung, Combinatorial effects on clumped isotopes and their significance in biogeochemistry. Geochim. Cosmochim. Acta 172, 22–38 (2016).
- L. Y. Yeung, J. L. Ash, E. D. Young, Biological signatures in clumped isotopes of O₂. Science 348, 431–434 (2015).
- E. D. Young, I. E. Kohl, B. Sherwood Lollar, G. Etiope, D. Rumble III, S. Li, M. A. Haghnegahdar,
 E. A. Schauble, K. A. McCain, D. I. Foustoukos, C. Sutclife, O. Warr, C. J. Ballentine,
 T. C. Onstott, H. Hosgormez, A. Neubeck, J. M. Marques, I. Pérez-Rodríguez, A. R. Rowe,
 - D. E. LaRowe, C. Magnabosco, L. Y. Yeung, J. L. Ash, L. T. Bryndzia, The relative abundances of resolved ¹²CH₂D₂ and ¹³CH₃D and mechanisms controlling isotopic bond ordering in abiotic and biotic methane gases. *Geochim. Cosmochim. Acta* **203**, 235–264 (2017).
- E. D. Young, D. Rumble III, P. Freedman, M. Mills, A large-radius high-mass-resolution multiple-collector isotope ratio mass spectrometer for analysis of rare isotopologues of O₂, N₂, CH₄ and other gases. *Int. J. Mass Spectrom.* 401, 1–10 (2016).

- L. Froidevaux, N. J. Livesey, W. G. Read, Y. B. Jiang, C. Jimenez, M. J. Filipiak, M. J. Schwartz, M. L. Santee, H. C. Pumphrey, J. H. Jiang, D. L. Wu, G. L. Manney, B. J. Drouin, J. W. Waters, E. J. Fetzer, P. F. Bernath, C. D. Boone, K. A. Walker, K. W. Jucks, G. C. Toon, J. J. Margitan, B. Sen, C. R. Webster, L. E. Christensen, J. W. Elkins, E. Atlas, R. A. Lueb, R. Hendershot, Early validation analyses of atmospheric profiles from EOS MLS on the Aura satellite. IEEE Trans. Geosci. Remote Sens. 44, 1106–1121 (2006).
- A. A. Wiegel, A. S. Cole, K. J. Hoag, E. L. Atlas, S. M. Schauffler, K. A. Boering, Unexpected variations in the triple oxygen isotope composition of stratospheric carbon dioxide. *Proc. Natl. Acad. Sci. U.S.A.* 110, 17680–17685 (2013).
- R. L. Sutka, N. E. Ostrom, P. H. Ostrom, J. A. Breznak, H. Gandhi, A. J. Pitt, F. Li, Distinguishing nitrous oxide production from nitrification and denitrification on the basis of isotopomer abundances. *Appl. Environ. Microbiol.* 72, 638–644 (2006).
- S. Toyoda, H. Mutobe, H. Yamagishi, N. Yoshida, Y. Tanji, Fractionation of N₂O isotopomers during production by denitrifier. Soil Biol. Biochem. 37, 1535–1545 (2005).
- S. M. Kotay, B. L. Mansell, M. Hogsett, H. Pei, R. Goel, Anaerobic ammonia oxidation (ANAMMOX) for side-stream treatment of anaerobic digester filtrate process performance and microbiology. *Biotechnol. Bioeng.* 110, 1180–1192 (2013).
- B. Brunner, S. Contreras, M. F. Lehmann, O. Matantseva, M. Rollog, T. Kalvelage,
 G. Klockgether, G. Lavik, M. S. M. Jetten, B. Kartal, M. M. M. Kuypers, Nitrogen isotope effects induced by anammox bacteria. *Proc. Natl. Acad. Sci. U.S.A.* 110, 18994–18999 (2013).
- L. Y. Yeung, E. D. Young, E. A. Schauble, Measurements of ¹⁸O¹⁸O and ¹⁷O¹⁸O in the atmosphere and the role of isotope-exchange reactions. *J. Geophys. Res.* 117, D18306 (2012)
- A. M. Grachev, J. P. Severinghaus, Laboratory determination of thermal diffusion constants for ²⁹N₂/²⁸N₂ in air at temperatures from -60 to 0°C for reconstruction of magnitudes of abrupt climate changes using the ice core fossil-air paleothermometer. Geochim. Cosmochim. Acta 67, 345-360 (2003).
- S. Ishidoya, S. Sugawara, S. Morimoto, S. Aoki, T. Nakazawa, Gravitational separation of major atmospheric components of nitrogen and oxygen in the stratosphere. *Geophys. Res. Lett.* 35, L03811 (2008).
- A. O. Nier, M. B. McElroy, Y. L. Yung, Isotopic composition of the Martian atmosphere. Science 194, 68–70 (1976).
- M. H. Wong, S. K. Atreya, P. N. Mahaffy, H. B. Franz, C. Malespin, M. G. Trainer, J. C. Stern, P. G. Conrad, H. L. Manning, R. O. Pepin, R. H. Becker, C. P. McKay, T. C. Owen, R. Navarro-González, J. H. Jones, B. M. Jakosky, A. Steele, Isotopes of nitrogen on Mars: Atmospheric measurements by Curiosity's mass spectrometer. *Geophys. Res. Lett.* 40, 6033–6037 (2013).
- H. B. Niemann, S. K. Atreya, J. E. Demick, D. Gautier, J. A. Haberman, D. N. Harpold, W. T. Kasprzak, J. I. Lunine, T. C. Owen, F. Raulin, Composition of Titan's lower atmosphere and simple surface volatiles as measured by the Cassini-Huygens probe gas chromatograph mass spectrometer experiment. J. Geophys. Res. 115, E12006 (2010).
- S. Chakraborty, B. H. Muskatel, T. L. Jackson, M. Ahmed, R. D. Levine, M. H. Thiemens, Massive isotopic effect in vacuum UV photodissociation of N₂ and implications for meteorite data. *Proc. Natl. Acad. Sci. U.S.A.* 111, 14704–14709 (2014).
- P. Croteau, J. B. Randazzo, O. Kostko, M. Ahmed, M.-C. Liang, Y. L. Yung, K. A. Boering, Measurements of isotope effects in the photoionization of N₂ and implications for Titan's atmosphere. Astrophys. J. Lett. 728, L32 (2011).
- 27. B. H. Muskatel, F. Remacle, M. H. Thiemens, R. D. Levine, On the strong and selective isotope effect in the UV excitation of N_2 with implications toward the nebula and Martian atmosphere. *Proc. Natl. Acad. Sci. U.S.A.* **108**, 6020–6025 (2011).
- K.-I. Matsushita, R. S. Hansen, Adsorption of activated nitrogen on tungsten. J. Chem. Phys. 52, 3619–3625 (1970).
- J. C. lanni, A comparison of the Bader-Deuflhard and the Cash-Karp Runge-Kutta integrators for the GRI-MECH 3.0 model based on the chemical kinetics code Kintecus, in Computational Fluid and Solid Mechanics 2003, K.-J. Bathe, Ed. (Elsevier Science Ltd., 2003), pp. 1368–1372.
- H.-L. Liu, B. T. Foster, M. E. Hagan, J. M. McInerney, A. Maute, L. Qian, A. D. Richmond, R. G. Roble, S. C. Solomon, R. R. Garcia, D. Kinnison, D. R. Marsh, A. K. Smith, J. Richter, F. Sassi, J. Oberheide, Thermosphere extension of the whole atmosphere community climate model. J. Geophys. Res. 115, A12302 (2010).
- J.T. Emmert, M. H. Stevens, P. F. Bernath, D. P. Drob, C. D. Boone, Observations of increasing carbon dioxide concentration in Earth's thermosphere. *Nat. Geosci.* 5, 868–871 (2012).
- J. Yue, J. Russell III, Y. Jian, L. Rezac, R. Garcia, M. López-Puertas, M. G. Mlynczak, Increasing carbon dioxide concentration in the upper atmosphere observed by SABER. Geophys. Res. Lett. 42, 7194–7199 (2015).
- E. A. Davidson, S. Seitzinger, The enigma of progress in denitrification research. Ecol. Appl. 16, 2057–2063 (2006).
- B. Marty, L. Zimmermann, Volatiles (He, C, N, Ar) in mid-ocean ridge basalts: Assesment of shallow-level fractionation and characterization of source composition. *Geochim. Cosmochim. Acta* 63, 3619–3633 (1999).
- R. K. Mohapatra, D. Harrison, U. Ott, J. D. Gilmour, M. Trieloff, Noble gas and nitrogen isotopic components in Oceanic Island Basalts. Chem. Geol. 266, 29–37 (2009).

- L. J. Elkins, T. P. Fischer, D. R. Hilton, Z. D. Sharp, S. McKnight, J. Walker, Tracing nitrogen in volcanic and geothermal volatiles from the Nicaraguan volcanic front. *Geochim. Cosmochim. Acta* 70, 5215–5235 (2006).
- Y. Li, B. Marty, S. Shcheka, L. Zimmermann, H. Keppler, Nitrogen isotope fractionation during terrestrial core-mantle separation. Geochem. Perspect. Lett. 2, 138–147 (2016).
- 38. G. K. Boreskov, Heterogeneous Catalysis (Nova Science Publications Inc., 2003), 236 pp.
- S. Toyoda, N. Yoshida, Determination of nitrogen isotopomers of nitrous oxide on a modified isotope ratio mass spectrometer. *Anal. Chem.* 71, 4711–4718 (1999).
- L. Y. Yeung, H. P. Affek, K. J. Hoag, W. Guo, A. A. Wiegel, E. L. Atlas, S. M. Schauffler, M. Okumura, K. A. Boering, J. M. Eiler, Large and unexpected enrichment in stratospheric ¹⁶O¹³C¹⁸O and its meridional variation. *Proc. Natl. Acad. Sci. U.S.A.* **106**, 11496–11501 (2009).
- L. Y. Yeung, L. T. Murray, J. L. Ash, E. D. Young, K. A. Boering, E. L. Atlas, S. M. Schauffler, R. A. Lueb, R. L. Langenfelds, P. B. Krummel, L. P. Steele, S. D. Eastham, Isotopic ordering in atmospheric O₂ as a tracer of ozone photochemistry and the tropical atmosphere. *J. Geophys. Res. Atmos.* 121, 12541–12559 (2016).
- S. Emerson, P. D. Quay, C. Stump, D. Wilbur, M. Knox, O₂, Ar, N₂, and ²²²Rn in surface waters of the subarctic ocean: Net biological O₂ production. *Global Biogeochem. Cycles* 5, 49–69 (1991).
- I. C. Anderson, M. Poth, J. Homstead, D. Burdige, A comparison of NO and N₂O production by the autotrophic nitrifier Nitrosomonas europaea and the heterotrophic nitrifier Alcaligenes faecalis. Appl. Environ. Microbiol. 59, 3525–3533 (1993).
- R. Rippka, J. Deruelles, J. B. Waterbury, M. Herdman, R. Y. Stanier, Generic assignments, strain histories and properties of pure cultures of cyanobacteria. *Microbiology* 111, 1–61 (1979).
- R. J. Ritchie, Consistent sets of spectrophotometric chlorophyll equations for acetone, methanol and ethanol solvents. *Photosynth. Res.* 89, 27–41 (2006).
- F. D. Colegrove, W. B. Hanson, F. S. Johnson, Eddy diffusion and oxygen transport in the lower thermosphere. J. Geophys. Res. 70, 4931–4941 (1965).
- M. G. Prokopenko, O. M. Pauluis, J. Granger, L. Y. Yeung, Exact evaluation of gross photosynthetic production from the oxygen triple-isotope composition of O₂: Implications for the net-to-gross primary production ratios. Geophys. Res. Lett. 38. L14603 (2011).
- X. Zhang, D. M. Sigman, F. M. M. Morel, A. M. L. Kraepiel, Nitrogen isotope fractionation by alternative nitrogenases and past ocean anoxia. *Proc. Natl. Acad. Sci. U.S.A.* 111, 4782–4787 (2014).
- E. D. Young, A. Galy, H. Nagahara, Kinetic and equilibrium mass-dependent isotope fractionation laws in nature and ther geochemical and cosmochemical significance. *Geochim. Cosmochim. Acta* 66, 1095–1104 (2002).
- M. Gilibert, A. Aguilar, M. González, F. Mota, R. Sayós, Dynamics of the N(⁴S_u) + NO(X ²Π) → N₂(X ¹Σ_g⁺) + O(³P_g) atmospheric reaction on the ³A' ground potential energy surface. I. Analytical potential energy surface and preliminary quasiclassical trajectory calculations. J. Chem. Phys. 97, 5542–5553 (1992).
- 51. Y. Q. Gao, R. A. Marcus, Strange and unconventional isotope effects in ozone formation. *Science* **293**, 259–263 (2001).
- M. H. Thiemens, J. E. Heidenreich III, The mass-independent fractionation of oxygen: A novel isotope effect and its possible cosmochemical implications. Science 219, 1073–1075 (1983).
- A. L. Buchachenko, Magnetic isotope effect: Nuclear spin control of chemical reactions. J. Phys. Chem. A 105, 9995–10011 (2001).
- N. Dauphas, E. A. Schauble, Mass fractionation laws, mass-independent effects, and isotopic anomalies. Annu. Rev. Earth Planet. Sci. 44, 709–783 (2016).
- 55. T. R. Govers, C. A. van de Runstraat, F. J. de Heer, Isotope effects in the predissociation of the $C^2\Sigma_u^+$ state of N_2^+ . *J. Phys. B At. Mol. Opt. Phys.* **6**, L73 (1973).
- 56. A. L. Roche, J. Tellinghuisen, Predissociation and perturbations in the $C^2\Sigma_u^+$ state of N_2^+ from interaction with the $B^2\Sigma_u^+$ state. *Mol. Phys.* **38**, 129–143 (1979).
- 57. C. A. van de Runstraat, F. J. de Heer, T. R. Govers, Excitation and decay of the $C^2\Sigma_u^+$ state of N_2^+ in the case of electron impact on N_2 . Chem. Phys. 3, 431–450 (1974).
- T. E. Van Zandt, T. F. O'Malley, Rate coefficient for the reaction of O⁺ with vibrationally excited N₂. J. Geophys. Res. 78, 6818–6820 (1973).
- L. Campbell, D. C. Cartwright, M. J. Brunger, P. J. O. Teubner, Role of electronic excited N₂ in vibrational excitation of the N₂ ground state at high latitudes. *J. Geophys. Res.* 111. A09317 (2006).
- M. R. Torr, D. G. Torr, P. G. Richards, The N₂⁺ first negative system in the dayglow from Spacelab 1. J. Geophys. Res. 97, 17075–17095 (1992).

- W. A. Abdou, D. G. Torr, P. G. Richards, M. R. Torr, E. L. Breig, Results of a comprehensive study of the photochemistry of N₂⁺ in the ionosphere. *J. Geophys. Res.* 89, 9069–9079 (1984)
- M. Gilibert, A. Aguilar, M. González, R. Sayós, Dynamics of the N(⁴S_u)+NO(X²Π)→ N₂(X¹Σ⁺g)+O(²P_g) atmospheric reaction on the ³A' ground potential energy surface.
 The effect of reagent translational, vibrational, and rotational energies. J. Chem. Phys. 99, 1719–1733 (1993).
- S. K. Solanki, N. A. Krivova, J. D. Haigh, Solar irradiance variability and climate. *Annu. Rev. Astron. Astrophys.* 51, 311–351 (2013).
- R. G. Roble, E. C. Ridley, R. E. Dickinson, On the global mean structure of the thermosphere.
 J. Geophys. Res. 92, 8745–8758 (1987).
- J. N. Bahcall, M. H. Pinsonneault, S. Basu, Solar models: Current epoch and time dependences, neutrinos, and helioseismological properties. Astrophys. J. 555, 990–1012 (2001).
- S. C. Cande, D. V. Kent, Revised calibration of the geomagnetic polarity timescale for the Late Cretaceous and Cenozoic. J. Geophys. Res. 100, 6093

 –6095 (1995).
- M. Sinnhuber, J. P. Burrows, M. P. Chipperfield, C. H. Jackman, M.-B. Kallenrode, K. F. Künzi, M. Quack, A model study of the impact of magnetic field structure on atmospheric composition during solar proton events. *Geophys. Res. Lett.* 30, 1818 (2003).
- M. McFarland, D. L. Albritton, F. C. Fehsenfeld, E. E. Ferguson, A. L. Schmeltekopf, Energy dependence and branching ratio of the N₂⁺ + O reaction. *J. Geophys. Res.* 79, 2925–2926 (1974).
- N. S. Shuman, D. E. Hunton, A. A. Viggiano, Ambient and modified atmospheric ion chemistry: From top to bottom. *Chem. Rev.* 115, 4542–4570 (2015).
- S. P. Sander, J. Abbatt, J. R. Barker, J. B. Burkholder, R. R. Friedl, D. M. Golden, R. E. Huie, C. E. Kolb, M. J. Kurylo, G. K. Moortgat, V. L. Orkin, P. H. Wine, Chemical Kinetics and Photochemical Data for Use in Atmospheric Studies: Evaluation Number 17, JPL Publication 10-6, NASA, Ed. (Jet Propulsion Laboratory, 2011).
- M. A. A. Clyne, D. H. Stedman, Rate of recombination of nitrogen atoms. J. Phys. Chem. 71, 3071–3073 (1967).
- I. M. Campbell, C. N. Gray, Rate constants for O(³P) recombination and association with N(⁴S). Chem. Phys. Lett. 18, 607–609 (1973).
- W. Tsang, R. F. Hampson, Chemical kinetic data base for combustion chemistry. Part I. Methane and related compounds. J. Phys. Chem. Ref. Data 15, 1087–1279 (1986).

Acknowledgments: We thank K. Boering (University of California, Berkeley) for providing a sample of stratospheric air for analysis; R. Goel (University of Utah) for providing samples from his anammox reactor; N. Rollins, T. Gunderson, W. Berelson (University of Southern California), and the crew of the R/V Yellowfin for assistance in acquiring seawater samples; and A. Ridley (University of Michigan) and M. Blomberg (Stockholm University) for helpful discussions. T.P.F. thanks the National Park Service for permits to collect samples at Yellowstone. Funding: This research was supported by NSF grants OCE-1533501 (to L.Y.Y.), EAR-1349182 (to L.Y.Y. and E.D.Y), EAR-1348935 (to N.E.O.), and EAR-1530306 (to E.A.S.). We also acknowledge support from grants from the Deep Carbon Observatory (UCLA) and the Department of Energy Great Lakes Bioenergy Research Center (DOE Office of Science, BER DE-FC02-07ER64494). Author contributions: L.Y.Y., N.E.O., and E.D.Y. designed the study. S.L., I.E.K., L.Y.Y., and E.D.Y. performed isotopic analyses and electrolysis experiments. J.A.H. and N.E.O. performed biological culturing experiments, T.P.F. sampled and analyzed the chemical composition of fumarole gases. H.H. sampled and isolated dissolved gases from seawater. E.A.S. performed theoretical calculations, L.Y.Y. built the chemical kinetic model of the electrolysis experiments and analyzed WACCM-X outputs. L.Y.Y. analyzed the data and wrote the manuscript with input from all the coauthors. Competing interests: The authors declare that they have no competing interests. Data and materials availability: The data used in this study are available in the Supplementary Materials (tables S1 to S6) and are permanently archived in the Rice

Submitted 14 August 2017 Accepted 26 October 2017 Published 17 November 2017 10.1126/sciadv.aao6741

the authors

Citation: L. Y. Yeung, S. Li, I. E. Kohl, J. A. Haslun, N. E. Ostrom, H. Hu, T. P. Fischer, E. A. Schauble, E. D. Young, Extreme enrichment in atmospheric ¹⁵N¹⁵N. *Sci. Adv.* **3**, eaao6741 (2017).

Digital Scholarship Archive. Additional data related to this paper may be requested from



Extreme enrichment in atmospheric ¹⁵N¹⁵N

Laurence Y. Yeung, Shuning Li, Issaku E. Kohl, Joshua A. Haslun, Nathaniel E. Ostrom, Huanting Hu, Tobias P. Fischer, Edwin A. Schauble and Edward D. Young

Sci Adv 3 (11), eaao6741. DOI: 10.1126/sciadv.aao6741

ARTICLE TOOLS http://advances.sciencemag.org/content/3/11/eaao6741

SUPPLEMENTARY MATERIALS http://advances.sciencemag.org/content/suppl/2017/11/13/3.11.eaao6741.DC1

REFERENCES

This article cites 70 articles, 14 of which you can access for free http://advances.sciencemag.org/content/3/11/eaao6741#BIBL

PERMISSIONS http://www.sciencemag.org/help/reprints-and-permissions

Use of this article is subject to the Terms of Service



advances.sciencemag.org/cgi/content/full/3/11/eaao6741/DC1

Supplementary Materials for

Extreme enrichment in atmospheric ¹⁵N¹⁵N

Laurence Y. Yeung, Shuning Li, Issaku E. Kohl, Joshua A. Haslun, Nathaniel E. Ostrom, Huanting Hu, Tobias P. Fischer, Edwin A. Schauble, Edward D. Young

Published 17 November 2017, *Sci. Adv.* **3**, eaao6741 (2017) DOI: 10.1126/sciadv.aao6741

This PDF file includes:

- Supplementary Text
- fig. S1. Theoretical Δ_{30} values at isotopic equilibrium ($\Delta_{30,\text{equil}}$) as a function of temperature, from Wang *et al.* (7).
- fig. S2. Analytical tests of Δ_{30} accuracy.
- fig. S3. Changes in visible emission properties during electrolysis experiments.
- fig. S4. Modeled gross rates of bond-breaking (black symbols) and bond-making (red symbols) reactions in the electrolysis experiments.
- table S1. Isotopic data for air samples and heated gases.
- table S2. Isotopic data for biological experiments.
- table S3. Data for electrolysis experiments.
- table S4. Reactions used in the model of the electrolysis experiments.
- table S5. Data for volcanic N_2 samples and end members used to derive mixing fractions f_{RS} and f_{mantle} .
- table S6. Results from diffusion experiment for verifying instrumental accuracy.
- References (47–73)

Supplementary Text

Determining the isotopic balance between atmospheric chemistry and biological cycling. The evolution of nitrogen within a single, well-mixed atmospheric box is captured by the following equation

$$\frac{d[N_2]}{dt} = F_{DN} - F_{N2fix} - k_{thermo} ([N_2] - [N_{2,thermo}])$$
(7)

where [N₂] is the mean atmospheric concentration of N₂ at given time, F represents the fluxes (mol yr⁻¹) due to nitrogen fixation (F_{N2fix}) and denitrification/anammox (F_{DN}), k_{thermo} represents the rate coefficient for N₂ recycling in the atmosphere (yr⁻¹; it occurs primarily in the thermosphere), and [N_{2,thermo}] represents the N₂ concentration when atmospheric N₂ recycling alone is allowed to reach steady state. This equation corresponds closely with the equation describing the biogeochemical O₂ budget of the oceanic mixed layer (47) in both form and concept: the well-mixed box contains a source (denitrification vs. photosynthesis), a sink (N₂ fixation vs. respiration), and a term that restores the material in the box toward a steady state (atmospheric cycling vs. air-water gas exchange). We thus simplify eq. 7 using analogous logic using ${}^*R_{atm} = {}^{15}R_{atm}$, ${}^{29}R_{atm}$ or ${}^{30}R_{atm}$ to represent the ${}^{15}N/{}^{14}N$, ${}^{29}N_2/{}^{28}N_2$ and ${}^{30}N_2/{}^{28}N_2$ ratios in the atmosphere, respectively, at a given time. The mass balance for *N_2 can then be written as

$$\frac{d^* R_{atm}[N_2]}{dt} = F_{DN}^* R_{DN} - F_{N2 fix}^* R_{atm}^* \alpha_{N2 fix} - k_{thermo} ([N_2]^* R_{atm} - [N_{2,thermo}]^* R_{thermo})$$
(8)

in which ${}^*\alpha_{N2fix}$ is the isotopic fractionation factor for N_2 fixation. Using the differential chain rule

$$\frac{d^* R_{atm}[N_2]}{dt} = {}^* R_{atm} \frac{d[N_2]}{dt} + [N_2] \frac{d^* R_{atm}}{dt}$$
(9)

and simplifying using the identity $1/{^*R_{atm}}(d^*R_{atm}/dt) = d(\ln {^*R_{atm}})/dt$, equations 7 and 8 can be combined to make

$$[N_{2}]\frac{dln({}^{*}R_{atm})}{dt} = F_{DN}\frac{{}^{*}R_{DN} - {}^{*}R_{atm}}{{}^{*}R_{atm}} + F_{N2 fix}(1 - {}^{*}\alpha_{N2 fix}) + k_{thermo}[N_{2,thermo}]\frac{{}^{*}R_{thermo} - {}^{*}R_{atm}}{{}^{*}R_{atm}}$$

$$(10)$$

Next we make an approximation of the definition of $\Delta_{30} \equiv ({}^{30}R/{}^{15}R^2-1)$, namely, recognizing that $ln (1 + \Delta_{30}) \approx \Delta_{30}$, which is accurate to within 0.2% for $\Delta_{30} = 20$ %. The definition of Δ_{30} can then be recast as

$$\Delta_{30} \approx ln \left[\frac{^{30}R}{\left(^{15}R\right)^2} \right] = ln\left(^{30}R\right) - 2ln\left(^{15}R\right)$$
 (11)

And its rate of change expressed as

$$\frac{d\Delta_{30}}{dt} = \frac{d\ln(^{30}R)}{dt} - 2\frac{d\ln(^{15}R)}{dt}$$
 (12)

Substituting eqs. 10 and 12 into eq. 8, we obtain

$$\left[N_{2} \right] \frac{d\Delta_{30}}{dt} = F_{DN} \left(\frac{^{30}R_{DN} - ^{30}R_{atm}}{^{30}R_{atm}} - 2 \frac{^{15}R_{DN} - ^{15}R_{atm}}{^{15}R_{atm}} \right) + F_{N2 fix} \left[\left(1 - ^{30}\alpha_{N2 fix} \right) - 2 \left(1 - ^{15}\alpha_{N2 fix} \right) \right]$$

$$+ k_{thermo} \left[N_{2,thermo} \right] \left(\frac{^{30}R_{thermo} - ^{30}R_{atm}}{^{30}R_{atm}} - 2 \frac{^{15}R_{thermo} - ^{15}R_{atm}}{^{15}R_{atm}} \right)$$

$$(13)$$

and at steady state in Δ_{30} value, we can solve for $F_{DN}/k_{\text{thermo}}[N_{2,\text{thermo}}]$

$$\frac{F_{DN}}{k_{thermo} \left[N_{2,thermo} \right]} = \frac{\left(\frac{^{30}R_{atm} - ^{30}R_{thermo}}{^{30}R_{atm}} - 2 \frac{^{15}R_{atm} - ^{15}R_{thermo}}{^{15}R_{atm}} \right)}{\left(\frac{^{30}R_{DN} - ^{30}R_{atm}}{^{30}R_{atm}} - 2 \frac{^{15}R_{DN} - ^{15}R_{atm}}{^{15}R_{atm}} \right) - \frac{F_{N2,fix}}{F_{DN}} \left[\left(1 - ^{30}\alpha_{N2,fix} \right) - 2 \left(1 - ^{15}\alpha_{N2,fix} \right) \right]}$$

$$\tag{14}$$

Using this more nuanced expression shows a dependence of the derived $F_{\rm DN}/k_{\rm thermo}[{\rm N}_{\rm 2,thermo}] = F_{\rm DN}/F_{\rm thermosphere}$ ratio on other factors including the bulk isotopic signatures of denitrification and atmospheric chemistry, as well as the balance between N₂ fixation and denitrification, F_{N2fix}/F_{DN} . However, the $F_{DN}/F_{\rm thermosphere}$ ratio depends weakly on the term containing F_{N2fix}/F_{DN} . Using a range for $^{15}\alpha_{N2fix}$ between 1.001 and 0.993 (48), and a plausible range of mass-dependent fractionation relationships [i.e., $^{30}\alpha_{N2fix} = (^{15}\alpha_{N2fix})^{\beta}$, where $\beta \approx 2$] (19, 49), we find that the nitrogen fixation term contributes <2% to the value of the denominator of eq. 14, even when F_{N2fix}/F_{DN} is varied by a factor of 2. Neglecting this term then yields

$$\frac{F_{DN}}{k_{thermo} \left[N_{2,thermo} \right]} \approx \frac{F_{bio}}{F_{thermosphere}} = \frac{\left(\frac{^{30}R_{atm} - ^{30}R_{thermo}}{^{30}R_{atm}} - 2\frac{^{15}R_{atm} - ^{15}R_{thermo}}{^{15}R_{atm}} \right)}{\left(\frac{^{30}R_{DN} - ^{30}R_{atm}}{^{30}R_{atm}} - 2\frac{^{15}R_{DN} - ^{15}R_{atm}}{^{15}R_{atm}} \right)} \tag{15}$$

which is equivalent to the expression $F_{\text{bio}}(\Delta_{30,\text{atm}} - \Delta_{30,\text{bio}}) + F_{\text{thermosphere}}(\Delta_{30,\text{atm}} - \Delta_{30,\text{thermosphere}}) \approx 0$ in the main text when $\Delta_{30,\text{bio}} = \Delta_{30,DN}$ and $^{15}R_{atm} = ^{15}R_{thermo} = ^{15}R_{DN}$. We note that due to the small amount of nitrogen in the thermosphere, $^{15}R_{atm} \approx ^{15}R_{thermo}$.

Mass-independent fractionation (MIF) and the cause of Δ_{30} increases during electrolysis. The departures of electrolyzed N_2 from the mass fractionation curves shown in Fig. 1

suggest that MIF mechanisms may be relevant in the electrolysis experiments. However, MIF is not needed to establish large Δ_{30} values. Consider a two-reaction system consisting of a bond-breaking reaction and a bond-making reaction: To yield a $^{15}N^{15}N$ excess in N_2 , either the destruction of N_2 must disfavor $^{15}N^{-15}N$ bond rupture or the recombination of N_2 must favor $^{15}N^{-15}N$ bond formation, or both. In the first case, a $^{15}N^{15}N$ excess accumulates in the residual N_2 over time. In the second case, $^{15}N^{-15}N$ bonds are preferentially formed relative to $^{14}N^{-15}N$ bonds. After many rupture-reformation cycles, even subtle isotopic preferences can result in seemingly non-mass-dependent $^{15}N^{15}N$ excesses. The relative proportion of $^{15}N^{-15}N$ bonds in N_2 can change dramatically in this scenario despite the overall $^{15}N^{/14}N$ ratio remaining unchanged because of mass conservation. Combinations of mass-dependent processes can in principle yield N_2 with any Δ_{30} values once all the N-N bonds have been broken and remade, but whether large deviations in Δ_{30} values are plausible is not clear. Thus, while a non-mass-dependent fractionation mechanism seems likely, one is not strictly required to explain the experimental results.

Moreover, we can rule out several known MIF mechanisms as the cause of the large Δ_{30} values resulting from electrolysis. Low symmetry of the candidate reactions [e.g., C_s symmetry for N + NO (50)] rules out symmetry-based MIF effects such as those relevant to O₃ formation (51, 52). The marked increase in MIF magnitude in electrolysis of O₂ + N₂ mixtures rules out isotope-selective coupling between electronically excited states of N₂ (25, 27) as the cause of the most extreme ¹⁵N¹⁵N enrichments in our experiments. Magnetic isotope effects partition isotopes most dramatically between those that have a nuclear spin and those that do not (53); however, both ¹⁵N and ¹⁴N have nuclear spin ($I = \frac{1}{2}$ and 1, respectively). A quantitative theory for those effects is still lacking (54), so it is still unclear if they are relevant.

The gas-phase chemistry of vibrationally excited molecules is a possible route to unusual isotope effects in N_2 chemistry. For example, predissociation of the excited $N_2^+(C^2\Sigma_u^+)$ molecule displays non-mass-dependent effects due to vibronic coupling with the $B^2\Sigma_u^+$ state. While the sign of the effect is incorrect for a given vibrational state—e.g., the $C^2\Sigma_u^+(v=3)$ state has a $^{14}N^{15}N^{15}N$ destruction preference of 5:3 (55-57)—the predissociation rates are highly state-dependent. Consequently, the precise isotope effect depends on the vibrational state distribution of $N_2^+(C^2\Sigma_u^+)$. Vibronic coupling between ground- and excited-state potential energy surfaces, and the resulting (potentially vibrational state-dependent) isotopic branching ratios are likely also relevant to bimolecular reactions involving N_2 . This area may be a fruitful avenue for future research that may also be relevant to other planetary atmospheres.

Effects of nonthermal chemistry in the upper atmosphere on $F_{\rm thermosphere}$. Many species in the upper atmosphere are not at local thermodynamic equilibrium due to an influx of high energy particles combined with low intermolecular collision rates and relatively long radiative lifetimes. Consequently, species in the thermosphere may be electronically, vibrationally, and/or translationally excited in a manner inconsistent with the Boltzmann distribution. They are, in effect, hyperthermal. Both the distribution and magnitude of excited-state populations are expected to vary in response to variations in solar forcing

(e.g., solar wind, solar flares, etc.). Both N-N bond-breaking and N-N bond-making reactions could be affected.

Hyperthermal populations of N_2 and N_2^+ molecules can alter total rates of N_2 destruction because they differ substantially in reactivity from their ground-state counterparts. For example, the $N_2 + O^+ \rightarrow NO^+ + N$ reaction for modestly vibrationally excited N_2 molecules can be two orders of magnitude faster than the reactions in the vibrational ground state (58). The nonthermal population in the thermosphere above 130 km increases the effective rate of N_2 destruction by up to a factor of five (59). Similarly, the vibrational population distribution of N_2^+ is nonthermal in the thermosphere (60), potentially affecting rates of both chemical destruction by atomic oxygen and dissociative recombination with electrons (61). For the $N_2 + N_2 + N_3 + N_4 + N_4$

In these and other cases in which reactions occur hyperthermally, the reaction rates increase rather than decrease, resulting in faster N_2 cycling rates. The atmospheric N_2 recycling rate ($F_{\text{thermosphere}}$), therefore, is most likely an underestimate. In the extreme case in which $F_{\text{thermosphere}}$ is a factor of 8 larger than what we calculated, i.e., 88 Tmol N_2 yr⁻¹, then $\Delta_{30,\text{thermosphere}} \sim 23\%$ would be consistent with bottom-up estimates of F_{bio} .

Effects of variations in top-of-atmosphere radiative fluxes on $F_{\rm thermosphere}$. The sensitivity of $F_{\rm thermosphere}$ to variations in solar radiation may be quite different on short (e.g., 11-year solar cycle) and long (millions of years) timescales. On short timescales, the intensity of UV light that drives upper-atmospheric photochemistry, particularly in the ~100 nm range, can vary by 1–2 orders of magnitude (63) between solar maximum and solar minimum conditions. Active nitrogen species (e.g., N, NO) vary accordingly by a factor of ~10; atomic oxygen may vary slightly less (64). Our $F_{\rm thermosphere}$ estimate is based on the WACCM-X model year 2001, near the maximum for that solar cycle, so the timescale $F_{\rm thermosphere}$ is likely an overestimate with respect to the solar cycle mean. Simulations spanning at least one solar cycle would be informative in this regard.

On long timescales, the secular evolution of solar output and variations in Earth's magnetosphere are important considerations. The total solar luminosity has increased by $\sim 0.1\%$ in the past 10 Myr (65). In contrast, 27 magnetic reversals, including 4 cryptochrons, have occurred over the past 10 Myr (66). Such changes in Earth's magnetic field can affect atmospheric chemistry at least as far down as the stratosphere (67). It is not clear how important these events may be for $F_{\text{thermosphere}}$, but temporary deviations in atmospheric nitrogen cycling rates from the long-term mean during these events cannot be ruled out. The magnitude of this error is poorly constrained.

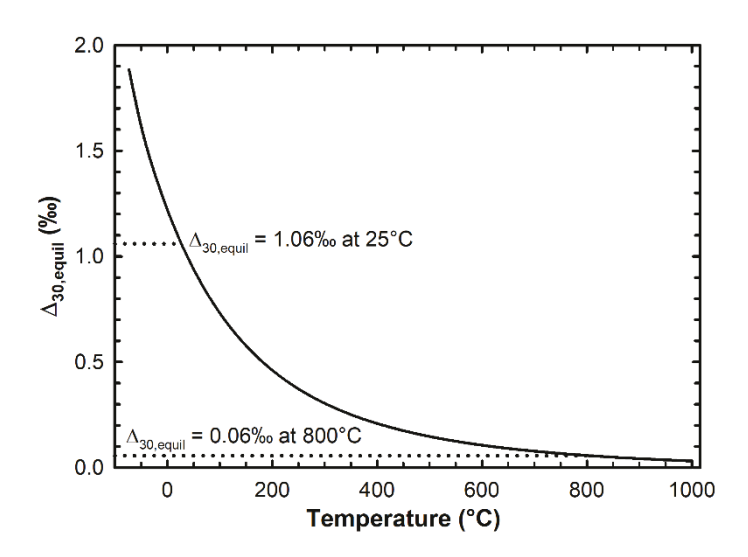


fig. S1. Theoretical Δ_{30} values at isotopic equilibrium ($\Delta_{30,equil}$) as a function of temperature, from Wang *et al.* (7). Shown also are numerical $\Delta_{30,equil}$ values at 25°C and 800°C.

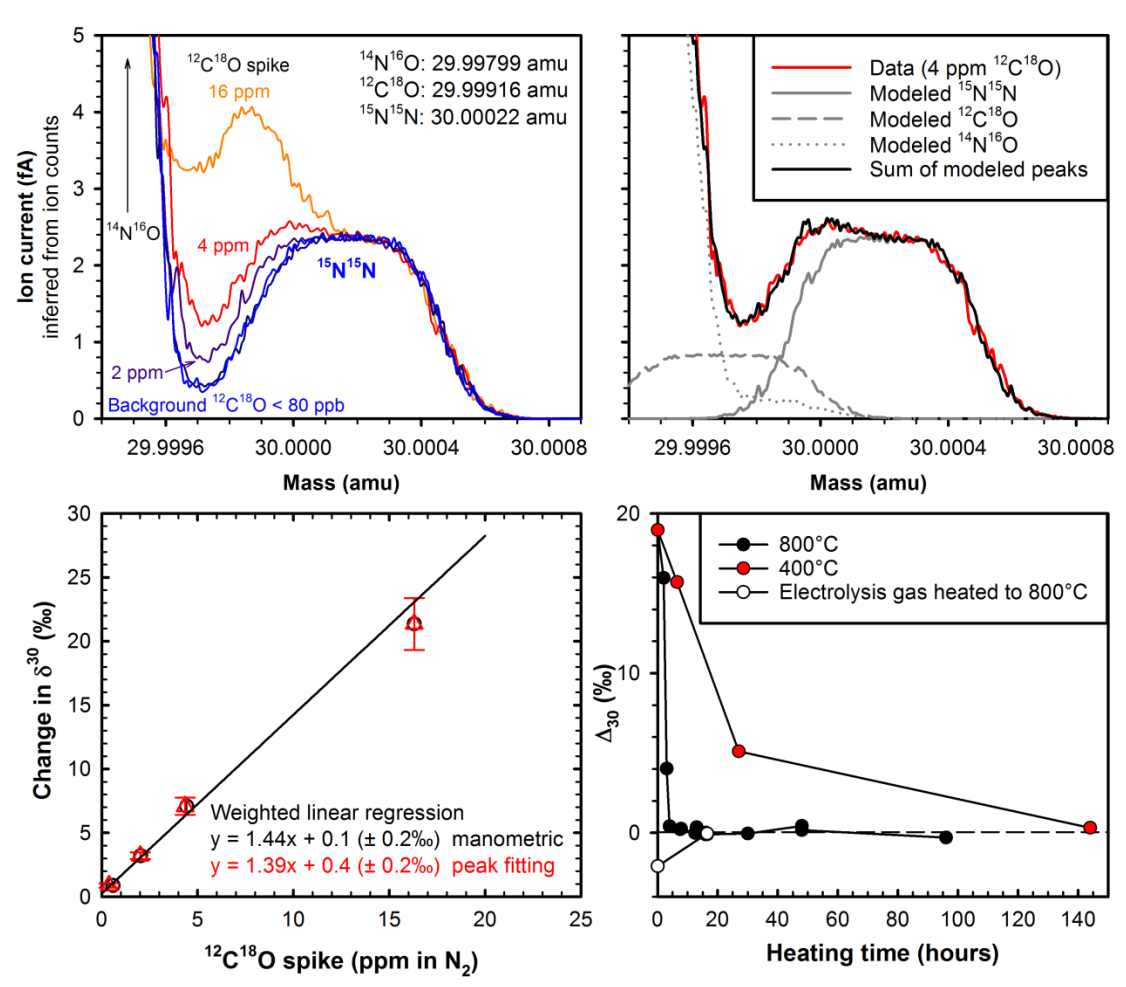


fig. S2. Analytical tests of Δ₃₀ **accuracy.** (*Top left*) Mass scans at m/z = 30 showing near-baseline resolution of 15 N 15 N $^{+}$ from 14 N 16 O $^{+}$ at a mass resolving power of 49,000 and contributions from a variable 12 C 18 O spike in the valley between them. (*Top right*) Example model of mass scan, for ~4 ppm 12 C 18 O spike in N₂, used to quantify the effect of the CO isobaric interference on Δ₃₀ values (*Bottom left*) Effect of 12 C 18 O on δ³⁰ value (≡ $^{30}R/^{28}R - 1$) determined using the standard-additions method. Results from manometric and peak-fitting measures of 12 C 18 O content agree within uncertainty. (*Bottom right*) Timed N₂ heating experiments over strontium nitride showing equilibration at 400°C and 800°C (Δ_{30,equil} = 0.21‰ and 0.06‰, respectively) from an initial Δ₃₀ value of 19‰, as well as including a sample that was equilibrated from an initial Δ₃₀ value of −2‰ generated by electrolysis.

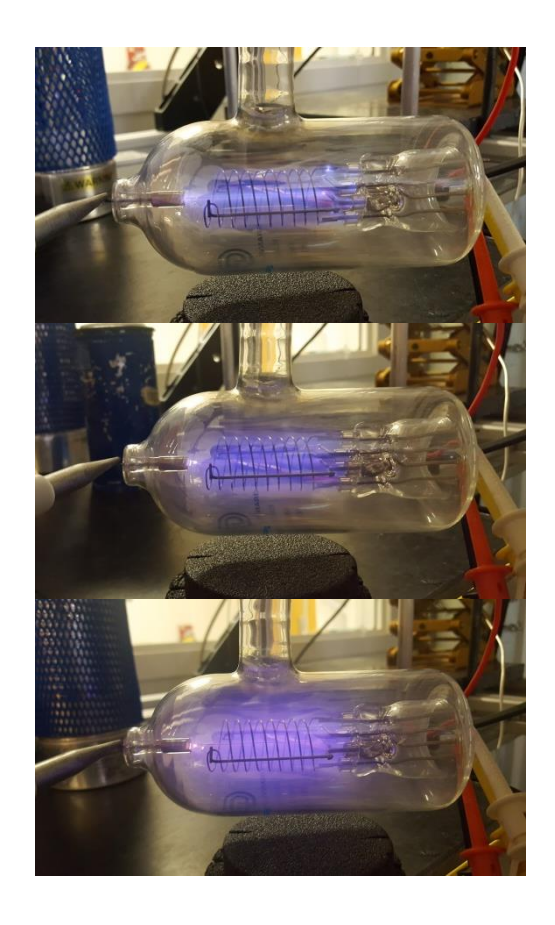


fig. S3. Changes in visible emission properties during electrolysis experiments. The emission becomes more diffuse as pressure decreases. Top to bottom: 21 mbar (N_2 only), 2.5 mbar (N_2 only), 1.0 mbar (1:3.7 O_2 : N_2).

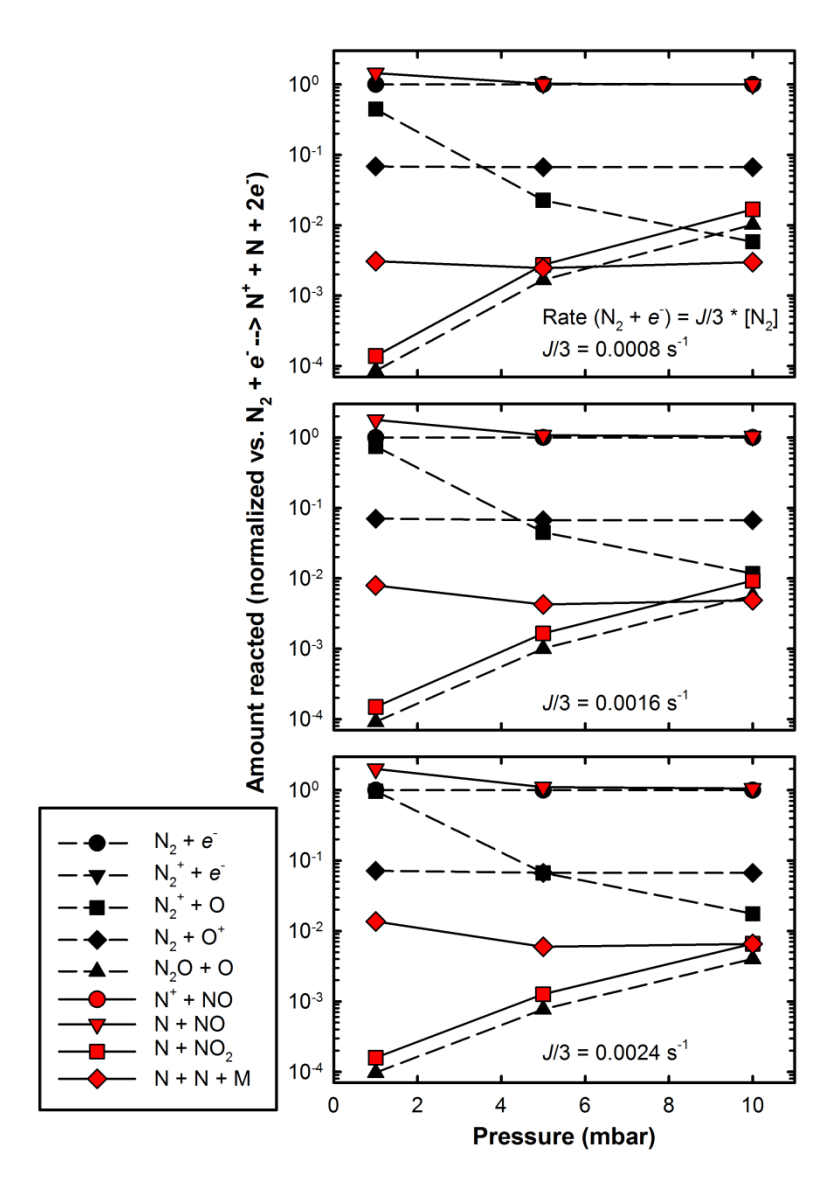


fig. S4. Modeled gross rates of bond-breaking (black symbols) and bond-making (red symbols) reactions in the electrolysis experiments. Rates are normalized to the rate of $N_2 + e^- \rightarrow N^+ + N + 2e^-$ for clarity across a range of reaction conditions. The three panels represent different electron number densities resulting in a threefold variation in the rate coefficient J/3 (see table S4).

table S1. Isotopic data for air samples and heated gases.

Sample	$\delta^{29}N_2 / \%_0$	$\delta^{30}N_2$ / ‰	δ ¹⁵ N / ‰	Δ ₃₀ / ‰	1 s.e. / %
UCLA air	-0.03	0.00	-0.03	19.3	0.1
	-0.04	-0.16	-0.04	19.1	0.1
	0.06	0.20	0.06	19.3	0.1
	0.02	-0.07	0.02	19.1	0.1
	0.03	0.21	0.03	19.4	0.1
	-0.03	-0.18	-0.03	19.1	0.1
	-0.02	-0.04	-0.02	19.1	0.2
	-0.05	0.03	-0.05	19.2	0.3
	0.01	0.18	0.01	19.2	0.2
	0.07	0.08	0.07	19.0	0.1
	-0.02	-0.24	-0.02	18.9	0.1
Stratospheric air (32 km)	-0.13	-0.06	-0.13	19.3	0.2
•	-0.07	-0.17	-0.07	19.1	0.1
Dissolved air (SPOT 29 m)*	0.66	1.62	0.66	19.0	0.1
Dissolved air (SPOT 10 m)*	0.61	1.28	0.61	18.7	0.1
Heated gas standards (800°C)	-7.64	-33.70	-7.71	0.2	0.1
, ,	-7.25	-33.18	-7.32	0.0	0.1
	-7.23	-33.15	-7.30	0.0	0.1
	-7.02	-32.56	-7.09	0.0	0.3
	-10.11	-38.67	-10.18	-0.1	0.4
	-9.98	-38.09	-10.05	0.3	0.3
	-3.46	-25.74	-3.53	-0.1	0.1
	-1.96	-22.74	-2.03	-0.0	0.1
	-3.13	-24.97	-3.20	0.0	0.1
	-4.27	-27.31	-4.34	-0.1	0.1

^{*}After correcting for ion-intensity effects, dissolved air samples Δ_{30} values were 19.4% (SPOT 29m) and 19.1% (SPOT 10m). No other samples were affected (see *Materials and Methods*). 1 s.e. = one standard error of the analysis.

table S2. Isotopic data for biological experiments.

Sample	$f^{^{*}}$	$\delta^{29}N_2/\%_0$	$\delta^{30}N_2/\%_0$	$\delta^{15}N$ / ‰	Δ_{30} / ‰	1 s.e. / %
P. stutzeri	0.85	-23.90	-63.86	-23.97	1.4	0.2
	0.74	-18.33	-53.68	-18.40	0.9	0.2
	0.59	-16.26	-49.55	-16.32	1.0	0.1
	0.15	-5.92	-30.06	-5.99	0.4	0.2
P. denitrificans	0.88	-29.55	-75.37	-29.61	0.7	0.1
•	0.83	-29.14	-74.33	-29.20	0.9	0.1
	0.61	-23.32	-63.62	-23.39	0.5	0.1
	0.62	-19.73	-56.83	-19.80	0.4	0.1
	0.44	-13.93	-45.59	-14.00	0.4	0.1
A. variabilis						
control	0.99	0.01	0.36	0.01	19.4	0.1
control	1.04	0.24	0.64	0.24	19.2	0.1
	1.10	0.21	0.22	0.21	18.9	0.1
	0.97	0.52	1.28	0.52	19.3	0.1
	0.93	0.58	0.97	0.58	18.9	0.1
	0.91	0.58	1.14	0.58	19.1	0.1
Anammox reactor		-1.38	-3.64	-1.38	18.2	0.1
		-0.53	-1.80	-0.53	18.3	0.1

^{*}Fraction of initial reagent remaining. *P. stutzeri* and *P. denitrificans* cultures were inoculated with 300 µmol KNO₃, while the *A. variabilis* culture consumed atmospheric N₂ that was dissolved in water (see *Materials and Methods*).

¹ s.e. = one standard error of the analysis.

table S3. Data for electrolysis experiments.

Sample	Pressure / mbar	$\delta^{29}N_2/\%_0$	$\delta^{30}N_2/\%_0$	$\delta^{15}N$ / ‰	Δ30 / ‰	1 s.e. / ‰
N ₂ only	1.3 [†]	-3.87	-20.17	-3.91	6.4	0.2
	2.5^{*}	-8.03	-27.50	-8.08	7.3	0.4
	2.5^{*}	0.04	-14.03	-0.01	4.8	0.1
	3.2^{\dagger}	-3.95	-19.94	-4.00	6.8	0.3
	3.2^{\dagger}	-1.64	-14.91	-1.68	7.3	0.4
	7.4^{*}	0.23	-16.29	0.17	2.1	0.2
	21.0^{*}	-0.16	-21.24	-0.24	-2.1	0.1
	23.6*	-0.33	-22.39	-0.41	-2.9	0.1
0.31 . (1.25)	1.0*	0.60	5 00	0.57	12.0	0.2
$O_2:N_2$ mix (1:3.7)	1.0*	0.60	-5.80	0.57	12.0	0.3
	3.3* 3.7 [†]	$0.05 \\ -3.35$	0.35 -6.49	$0.05 \\ -3.35$	19.3 19.3	0.1 0.2
O ₂ :N ₂ mix (1:1)						
No electrolysis (blank)	3.9^{\dagger}	-2.19	-23.24	-2.26	-0.1	0.2
, ,	3.7^{*}	-1.08	0.99	-1.07	22.3	0.2
	4.1^{\dagger}	-4.21	-4.86	-4.19	22.7	0.2
	4.7^{*}	-0.66	0.82	-0.65	21.2	0.2
	8.7†	-4.59	-12.62	-4.60	15.5	0.1
	11.0*	-0.58	-6.11	-0.60	14.1	0.1
$O_2:N_2 mix (2:1)$	2.7^{\dagger}	-3.89	-7.24	-3.89	19.6	0.3

^{*}Starting gas Δ_{30} = 19.0% †Starting gas Δ_{30} = 0%. 1 s.e. = one standard error of the analysis.

table S4. Reactions used in the model of the electrolysis experiments.

Reaction	Temperature-dependent rate expression*	Rate coefficient at 298K (cm ³ s ⁻¹)	Reference
N–N bond-breaking reactions			
$N_2 + e^- \rightarrow N_2^+ + 2e^-$		J	
\rightarrow N ⁺ + N + 2 e^-		J/3	
$N_2^+ + e^- \rightarrow 2N$	$1.8 \times 10^{-7} (300/T_e)^{0.39}$	4.6×10^{-8}	(64)
$N_2^+ + O \rightarrow NO^+ + N$	$[1 - 0.07*(300/T)^{0.21}]*1.4 \times 10^{-7}(300/T)^{0.44}$	1.3×10^{-10}	(68)
\rightarrow N ₂ + O ⁺	$0.07*(300/T)^{0.21}*1.4\times10^{-7}(300/T)^{0.44}$	9.8×10^{-12}	(68)
$N_2 + O^+ \rightarrow NO + N^+$	$1.4 \times 10^{-12} (300/T)^{1.1} + 1 \times 10^{-10} e^{-3280/T}$	1.4×10^{-12}	(69)
$N_2O + O \rightarrow N_2 + O_2$	$4.63 \times 10^{-11} e^{20/T}$	4.9×10^{-11}	$(70)^{\dagger}$
\rightarrow 2NO	$7.25 \times 10^{-11} e^{20/T}$	7.7×10^{-11}	(<i>70</i>) [†]
N-N bond-making reactions			
$N^+ + NO \rightarrow N_2^+ + O$	$0.15*5.1\times10^{-10}(300/T)^{0.4}$	7.7×10^{-11}	(69)
$N + NO \rightarrow N_2 + O$	$2.1 \times 10^{-11} e^{100/T}$	3.0×10^{-11}	(70)
$N + NO_2 \rightarrow N_2O + O$	$5.8 \times 10^{-12} e^{220/\text{T}}$	1.2×10^{-11}	(70)
$N + N + M \rightarrow N_2 + M$	$1.38 \times 10^{-33} e^{4182/\text{RT}}$	$7.4 \times 10^{-33} (\text{cm}^6 \text{s}^{-1})$	(71)
Other biomolecular reactions			
$O_2 + e^- \rightarrow O_2^+ + 2e^-$		J	
\rightarrow O ⁺ + O + 2 e^-		J/3	
$O_2^+ + e^- \rightarrow 2O$	$1.6 \times 10^{-7} (300/T_e)^{0.55}$	2.3×10^{-8}	(64)
$NO^+ + e^- \rightarrow N + O$	$4.2 \times 10^{-7} (300/T_e)^{0.85}$	2.1×10^{-8}	(64)
$N^+ + O_2 \rightarrow N + O_2^+$	$0.52*5.2\times10^{-10} + 5\times10^{-12}e^{-1098/T}$	2.7×10^{-10}	(69)
\rightarrow NO ⁺ + O	$0.40*5.2\times10^{-10} + 5\times10^{-12}e^{-1098/T}$	2.1×10^{-10}	(69)
\rightarrow NO + O ⁺	$0.08*5.2\times10^{-10} + 5\times10^{-12}e^{-1098/T}$	4.2×10^{-11}	(69)
$N^+ + O \rightarrow N + O^+$	1.0×10^{-12}	1.0×10^{-12}	(64)
$N_2^+ + O_2 \rightarrow N_2 + O_2^+$	$4\times10^{-11}(300/T)^{1.5} + 9\times10^{-11}e^{-1627/T}$	4.1×10^{-11}	(69)
$N_2^+ + NO \rightarrow N_2 + NO^+$	$4.1 \times 10^{-10} (300/T)^{0.6}$	4.1×10^{-10}	(69)
$N^+ + NO \rightarrow N + NO^+$	$0.85*5.1\times10^{-10}(300/T)^{0.4}$	4.3×10^{-10}	(69)
$N + O_2^+ \rightarrow NO^+ + O$		1.2×10^{-10}	(64)
	$2.82\times10^{-11} - 7.74\times10^{-12}(T/300) +$		
$O^+ + O_2 \rightarrow O_2^+ + O$	$1.073 \times 10^{-12} (T/300)^2 - 5.17 \times 10^{-14} (T/300)^3 + 9.65 \times 10^{-16} (T/300)^4$	2.2×10^{-11}	(64)
$O^+ + NO \rightarrow NO^+ + O$	$5.0 \times 10^{-13} (300/T)^{1.6} + 4 \times 10^{-12} e^{-448/T}$	1.4×10^{-12}	(69)
$O_2^+ + NO \rightarrow NO^+ + O_2$	1.4×10^{-10}	4.4×10^{-10}	(64)
$N + O_2 \rightarrow NO + O$	$1.5 \times 10^{-11} e^{-3600/T}$	8.5×10^{-17}	(70)
$N + O_3 \rightarrow NO + O_2$	$< 2.0 \times 10^{-16}$	2.0×10^{-16}	(70)‡
$O + O_3 \rightarrow 2O_2$	$8.0 \times 10^{-12} e^{-2060/T}$	8.0×10^{-15}	(70)
$NO + O_3 \rightarrow NO_2 + O_2$	$3.0 \times 10^{-11} e^{-1500/T}$	1.9×10^{-14}	(70)
$NO_2 + O_3 \rightarrow NO_3 + O_2$	$1.2 \times 10^{-13} e^{-2450/T}$	3.2×10^{-17}	(70)
$O + NO_2 \rightarrow NO + O_2$	$5.1 \times 10^{-12} e^{210/T}$	1.0×10^{-11}	(70)
$O + NO_3 \rightarrow O_2 + NO_2$	1.0×10^{-11}	1.0×10^{-11}	(70)
$NO + NO_3 \rightarrow 2NO_2$	$1.5 \times 10^{-11} e^{170/T}$	2.6×10^{-11}	(70)
$NO_3 + NO_3 \rightarrow 2NO_2 + O_2$	$8.5 \times 10^{-13} e^{-2450/T}$	2.3×10^{-16}	(70)
Other termolecular reactions			
$N + O + M \rightarrow NO + M$		$9.2 \times 10^{-33} (\text{cm}^6 \text{s}^{-1})$	(72)
$O + O + M \rightarrow O_2 + M$	$5.21 \times 10^{-35} e^{7480/\text{RT}}$	$1.0 \times 10^{-33} (\text{cm}^6 \text{s}^{-1})$	(73)
$O + O_2 + M \rightarrow O_3 + M$	$6.0 \times 10^{-34} (300/T)^{2.4}$	$6.1 \times 10^{-34} (\text{cm}^6 \text{s}^{-1})$	(70)
$O + NO + M \rightarrow NO_2 + M$	$9.0 \times 10^{-32} (300/T)^{-1.5}$	$9.1 \times 10^{-32} (\text{cm}^6 \text{s}^{-1})$	(70)§
$O + NO_2 + M \rightarrow NO_3 + M$	$2.5 \times 10^{-31} (300/T)^{-1.8}$	$2.5 \times 10^{-31} (\text{cm}^6 \text{s}^{-1})$	(70)§

*Thermal (T) and electron (T_e) temperatures in K. $^{\dagger}O(^{1}D)$ rate. ‡ upper limit. $^{\$}$ Rate calculated at low-pressure limit.

table S5. Data for volcanic N2 samples and end members used to derive mixing fractions f_{RS} and f_{mantle} .

N ₂ /He	δ^{15} N ± 1 s.e.	$\Delta_{30} \pm 1$ s.e.	$f_{ m RS}$		$f_{ m mantle}$	
	/ ‰	/ ‰	N ₂ /He	Δ_{30}	N ₂ /He	Δ_{30}
2133	5.41 ± 0.3	1.5 ± 0.3	0.94	0.91	0.06	0.09
1131	3.89 ± 0.3	3.9 ± 0.2	0.86	0.82	0.14	0.18
156	-1.82 ± 0.3	11.6 ± 0.3	0.19	0.03	0.81	0.97
	-1.63 ± 0.3	10.8 ± 0.5		0.11		0.89
1.489×10^{5}	0	19.1				
1.05×10^4	7	0.07				
124	-5	0.07				
	$ 2133 1131 156 $ $ 1.489 \times 10^{5} $ $ 1.05 \times 10^{4} $	N ₂ /He / $\frac{1}{2}$ / $\frac{1}{2$	N2/He / ‰ / ‰ 2133 5.41 ± 0.3 1.5 ± 0.3 1131 3.89 ± 0.3 3.9 ± 0.2 156 -1.82 ± 0.3 11.6 ± 0.3 -1.63 ± 0.3 10.8 ± 0.5 1.489×10^5 0 19.1 1.05×10^4 7 0.07	N2/He / %0 / 30 ± 1 s.c. 133 5.41 ± 0.3 1.5 ± 0.3 0.94 1131 3.89 ± 0.3 3.9 ± 0.2 0.86 156 -1.82 ± 0.3 11.6 ± 0.3 0.19 -1.63 ± 0.3 10.8 ± 0.5 1.489×10^5 0 19.1 1.05×10^4 7 0.07	N2/He /%0 /%0 N2/He Δ_{30} 2133 5.41 ± 0.3 1.5 ± 0.3 0.94 0.91 1131 3.89 ± 0.3 3.9 ± 0.2 0.86 0.82 156 -1.82 ± 0.3 11.6 ± 0.3 0.19 0.03 -1.63 ± 0.3 10.8 ± 0.5 0.11 1.489×10^5 0 19.1 1.05×10^4 7 0.07	N2/He /‰ /‰ N2/He Δ_{30} N2/He 2133 5.41 ± 0.3 1.5 ± 0.3 0.94 0.91 0.06 1131 3.89 ± 0.3 3.9 ± 0.2 0.86 0.82 0.14 156 -1.82 ± 0.3 11.6 ± 0.3 0.19 0.03 0.81 -1.63 ± 0.3 10.8 ± 0.5 0.11 1.489×10^5 0 19.1 1.05×10^4 7 0.07

table S6. Results from diffusion experiment for verifying instrumental accuracy.

Sample	Fraction not	Exper	riment	The	D /D	
	diffused, f	$\Delta\delta^{29}{N_2}^*/\ \%_0$	$\Delta\delta^{30}{N_2}^*/\%_0$	$\Delta\delta^{29}{N_2}^*/\%_0$	$\Delta\delta^{30}{N_2}^*/\%_0$	$P_{ m ds}/P_{ m us}$
Experiment 1 Experiment 2	0.483 0.529	21.19 20.65	41.37 40.74	21.10 20.73	41.36 40.60	0.14 0.12

 $^{^*\}Delta\delta^{29}N_2 = \delta^{29}N_{2,residue} - \delta^{29}N_{2,diffused} \text{ and } \Delta\delta^{30}N_2 = \delta^{30}N_{2,residue} - \delta^{30}N_{2,diffused}.$ †Includes correction for back-diffusion after ref. (19), with effective fractionation factor α_{eff} consistent with $\alpha_{eff} - 1 = (\alpha_{effusion} - 1)(1 - P_{ds}/P_{us}).$